THESIS FOR THE DEGREE OF DOCTOR OF PHILOSOPHY

Microwave measurement techniques for industrial process monitoring and quality control

JOHAN NOHLERT

CHALMERS

Department of Electrical Engineering
CHALMERS UNIVERSITY OF TECHNOLOGY
Göteborg, Sweden, 2018

Microwave measurement techniques for industrial process monitoring and quality control

JOHAN NOHLERT

ISBN 978-91-7597-700-3

Doktorsavhandlingar vid Chalmers Tekniska Högskola
Ny serie Nr 4381
ISSN 0346-718X

Department of Electrical Engineering
Signal Processing Group
Chalmers University of Technology
SE-412 96 Göteborg, Sweden

Telephone: +46 (0)31-772 1000

Cover: Illustration of cavity resonator measurements for monitoring of a fluidised bed process (left), and for detection of undesirable objects in a granular flow (right). The left illustration is created by Pernilla Börjesson.

This thesis has been prepared using LaTeX

Printed by Chalmers Reproservice
Göteborg, 2018

Till Hanna och Alma

MICROWAVE MEASUREMENT TECHNIQUES FOR INDUSTRIAL PROCESS MONITORING AND QUALITY CONTROL

JOHAN NOHLERT

Department of Electrical Engineering
Chalmers University of Technology

ABSTRACT

Process monitoring and quality control by sensor measurements are essential for the automatisation and optimisation of many industrial manufacturing processes. This thesis is concerned with microwave sensing, which is a measurement modality with potential to improve the in-line sensing capabilities in several industries. Two process-industrial measurement problems are considered that involve the estimation and detection of permittivity variations for granular media in a fluidised or flowing state. For these problems, we present microwave measurement techniques based on resonant cavity sensors, accounting for the electromagnetic design and modelling of the sensor, signal processing algorithms, and experimental evaluation in relevant industrial settings. These measurement techniques make simultaneous use of multiple resonant modes with spatial diversity to improve the measurement capabilities. Furthermore, we exploit model-based signal processing algorithms where knowledge of the underlying physics is utilised for improved estimation and detection.

The first problem is to monitor the internal state of a pharmaceutical fluidised bed process used for film-coating and drying of particles. The metal vessel that confines the process is here treated as a cavity resonator and the complex resonant frequency of eight different cavity modes are measured using a network analyser. Based on the resonant frequencies, we estimate parameters in a low-order model for the spatial permittivity distribution inside the vessel, which can be related to process states such as the liquid and solid content of the particles in different regions.

The second measurement problem is an aspect of quality control, namely the detection of undesirable objects in flowing granular materials. We present measurement techniques based on resonant cavity sensors that are capable to detect the presence of small dielectric objects embedded in a flowing granular material. Detection algorithms that exploit the statistics of the noise caused by material density fluctuations and the characteristic signatures caused by an object passage event, are evaluated based on experiments which lead to quantitative assessments of the detection performance.

Keywords: Microwave measurement, cavity resonator, fluidised bed, powder, finite element method, parameter estimation, signal detection, matched filter.

Preface

This thesis is for the degree of Doctor of Philosophy at Chalmers University of Technology. The work behind the thesis has been carried out within the Signal Processing group at the department of Electrical Engineering (formerly Signals and Systems) at Chalmers University, under the supervision of professor Thomas Rylander (main advisor and examiner) and professor Tomas McKelvey (co-advisor).

The work has been financially supported by the Swedish agency for innovation systems (VINNOVA) via the centres Chase and ChaseOn, with Food Radar Systems AB in Göteborg being an industrial partner. In addition, AstraZeneca R&D in Mölndal has been an industrial partner during part of the work.

Computations have been performed on resources at Chalmers Centre for Computational Science and Engineering (C3SE) provided by the Swedish National Infrastructure for Computing (SNIC).

List of appended papers

This thesis is based on the work contained in the following papers, referred to in the text by their roman numerals.

Paper I J. Nohlert, L. Cerullo, J. Winges, T. Rylander, T. McKelvey, A. Holmgren, L. Gradinarsky, S. Folestad, M. Viberg, and A. Rasmuson, "Global Monitoring of Fluidized-Bed Processes by means of Microwave Cavity Resonances", *Measurement*, vol. 55, pp. 520-535, 2014.

Paper II J. Nohlert, T. Rylander, and T. McKelvey, "Microwave Resonator Sensor for Detection of Dielectric Objects in Metal Pipes", *Proceedings of the 2015 IEEE International Instrumentation and Measurement Technology Conference (I2MTC)*, pp. 914-919, Pisa, 2015.

Paper III J. Nohlert, T. Rylander, and T. McKelvey, "Microwave Measurement System for Detection of Dielectric Objects in Powders", *IEEE Transactions on Microwave Theory and Techniques*, vol. 64, no. 11, pp. 3851-3863, 2016.

Paper IV J. Nohlert, T. Rylander, and T. McKelvey, "Matched Filter for Microwave-Based Detection of Dielectric Objects in Powders", *Proceedings of the 2017 IEEE International Instrumentation and Measurement Technology Conference (I2MTC)*, pp. 1-6, Torino, 2017.

Paper V J. Nohlert, T. Rylander, and T. McKelvey, "Cavity Resonator Sensor and Temporal Signals Analysis for Object Detection in Granular Flows", *Submitted to IEEE Transactions on Instrumentation and Measurement*, 2018.

Abbreviations and nomenclature

Abbreviations

ADC	Analogue to Digital Converter
API	Active Pharmaceutical Ingredient
AUC	Area Under an ROC-Curve
CEM	Computational Electromagnetics
CRLB	Cramér-Rao Lower Bound
DTFT	Discrete Time Fourier Transform
ECT	Electrical Capacitance Tomography
FDA	United States Food and Drug Administration
FDTD	Finite Difference Time Domain
FEM	Finite Element Method
GLRT	Generalised Likelihood Ratio Test
LDA	Linear Discriminant Analysis
LRT	Likelihood Ratio Test
LS	Least Squares
MAP	Maximum Aposteriori
MCC	Microcrystalline Cellulose
ML	Maximum Likelihood
MLE	Maximum Likelihood Estimator
MMSE	Minimum Mean Squared Error
MoM	Method of Moments
MUT	Material Under Test
MVU	Minimum Variance Unbiased
NIR	Near Infrared
PDF	Probability Density Function
PSD	Power Spectral Density
RF	Radio Frequency
ROC	Receiver Operating Characteristic
TE	Transverse Electric
TEM	Transverse Electromagnetic
TM	Transverse Magnetic
VCO	Voltage Controlled Oscillator
VNA	Vector Network Analyser
WSS	Wide Sense Stationary

Notational conventions

$\vec{X}$	Physical vector, real or complex
x	Scalar, real or complex
$\mathbf{x}$	Column vector in linear algebra context, real or complex
$\mathbf{X}$	Matrix, real or complex
$\hat{x}$	Estimate of x
$E[x]$	Expected value of x
$\mathrm{Re}\{x\}$	Real part of x
$\mathrm{Im}\{x\}$	Imaginary part of x
$\lvert x\rvert$	Absolute value of the real or complex scalar x
$\lvert\lvert\mathbf{x}\rvert\rvert$	Euclidean norm of the vector $\mathbf{x}$
x^*	Complex conjugate of x
$\mathbf{X}^{\mathrm{T}}$	Transpose of the matrix $\mathbf{X}$
$\mathbf{X}^{\mathrm{H}}$	Conjugate transpose of the matrix $\mathbf{X}$
$\det(\mathbf{X})$	Determinant of the matrix $\mathbf{X}$
j	Imaginary unit
$\mathbb{R}$	Set of real numbers
$\mathbb{C}$	Set of complex numbers

Symbols for common quantities and their SI units

$\vec{E}$	Electric field $(\mathrm{V/m})$
$\vec{D}$	Electric flux density $(\mathrm{As/m^2})$
$\vec{H}$	Magnetic field $(\mathrm{A/m})$
$\vec{B}$	Magnetic flux density $(\mathrm{Vs/m^2})$
$\vec{J}$	Volume current density $(\mathrm{A/m^2})$
ρ	Volume charge density $(\mathrm{As/m^3})$
ϵ	Absolute permittivity $(\mathrm{As/Vm})$
ϵ_0	Permittivity of vacuum $(\mathrm{As/Vm})$
ϵ_{r}	Relative permittivity
ϵ_{eff}	Effective permittivity $(\mathrm{As/Vm})$
μ	Absolute permeability $(\mathrm{Vs/Am})$
μ_0	Permeability of vacuum $(\mathrm{Vs/Am})$
f	Temporal frequency $(\mathrm{periods/s})$
ω	Angular frequency $(\mathrm{rad/s})$
Ω	Digital angular frequency $(\mathrm{rad/sample})$
ν	Volume fraction
Q	Quality factor
S_{pq}	Scattering parameter between ports p and q

Contents

Chapter 1

INTRODUCTION

The progress of modern industry brings a growing demand for advanced measurements to sense various properties of materials, processes and products. Automatised and optimised process control, enabled through accurate and reliable measurements of various process states, is a key for ensuring product quality, improving productivity and minimising environmental footprint for essentially any manufacturing industry. A common aim in many process industries is to monitor properties such as density, moisture content, particle size, purity and composition of solid, liquid, and granular materials (or a mixture of these) at different processing stages. This should preferably be done in-line, meaning that measurements are performed directly in the process flow and that the measurement result is obtained faster than the time by which the measured property may change. In-line functionality is vital if the sensing information is to be used for continuous process control. Furthermore, non-destructive measurements using sensors that do not disturb the process are advantageous or directly necessary in many industrial measurement problems.

One important measurement principle is to observe how an object responds to the exposure of an electromagnetic field – this is the basis for essentially all electromagnetic measurements. When categorised based on frequency, electromagnetic measurements range from quasi-static, via radio-frequency (RF) and microwave to optical, x-ray, and gamma-ray measurements. This thesis deals with microwave measurements, which employ electromagnetic waves that, upon interaction with the measurement object, are attenuated, phase-shifted or scattered. As a consequence, it is possible to infer various properties of a measurement object based on the microwave measurement response. The wavelength in the microwave region is often comparable to the size of the measurement object or the measurement domain (millimetres to metres), which may give rise to wave interference phenomena that can dramatically improve the measurement sensitivity. This is the basis for resonant microwave sensors, which is the sensor type considered in this thesis. Microwave sensing has several distinguishing aspects that are favourable for in-line process measurements. First, microwaves penetrate well through dielectric media which makes it possible to measure material bulk properties over a rep-

resentative volume, as opposed to optical techniques that provide only surface information for optically opaque media. Second, microwaves can be transmitted using probes or antennas located at a distance which enables contact-free measurements. Third, the high dielectric constant of water at microwave frequencies enables very sensitive moisture measurements. Fourth, microwaves at the power levels used for measurements (rarely exceeding 100 mW) are non-destructive to most materials and generally considered harmless to humans, and the measurements can be performed using relatively inexpensive measurement hardware.

The analysis and interpretation of sensor data by means of signal processing is, alongside with the electromagnetic aspects of the microwave sensor, an equally important aspect for a well-functioning measurement system. A significant part of this thesis is therefore devoted to model-based signal processing techniques for parameter estimation and classification where knowledge about the physical processes that underpins the observed microwave data is utilised.

1.1 Background and overview of the thesis

This thesis presents developments in the area of microwave-based measurement techniques for industrial applications, motivated by a need for new sensing capabilities in the process industry. Two industrial measurement problems have been studied, where the first is related to pharmaceutical process monitoring and the second to automatised quality control in material processing industries dealing with powders and granular materials. These problems have been addressed by considering the following aspects: (i) the electromagnetic design and behaviour of the sensor system; (ii) the development of signal processing algorithms to infer the desired measurement information from the sensor data; and (iii) the evaluation of the measurement system by means of industrially relevant experimental setups. In the following, a brief introduction to the application problems is presented whereas a more thorough discussion that includes the developed measurement systems can be found in Chapter 4 and in the appended papers.

In the first application problem that deals with pharmaceutical process monitoring, we consider the Wurster-type fluidised bed process which is illustrated in Fig. 1.1. This process is commonly used for film-coating of particles that are used in the manufacturing of solid oral dosage forms such as tablets and capsules. The particles are circulated inside a metal vessel where they are sprayed with a liquid that forms the coating layer as the solvent dries, which ideally occurs within one circulation. The coating film may contain an active pharmaceutical ingredient (API) or it can be designed to delay the release of an API in the digestive system or to protect API:s from ambient conditions during storage. Film-coated particles, possibly with several different functional layers, is therefore an important component in pharmaceutical products featuring controlled release of the active substances. The operating conditions of the coating process has important implications on the quality of the coating layer and hence on the final product, as well as the process yield and the consumption of energy and chemicals. It is therefore desirable to monitor the internal process states by means of in-line sensors in the strive towards real-time process control and optimisation. Furthermore, the use of

process-analytical technologies in pharmaceutical development and manufacturing is encouraged by regulatory agencies such as the United States Food and Drug Administration (FDA) [1]. One important process parameter to monitor is the moisture content of the particles in different spatial regions inside the vessel, and its evolution over time. In Paper I, we present a step towards this goal in terms of a microwave measurement system that exploits cavity resonances in the process vessel to estimate parameters in a low-order model for the spatial permittivity distribution.

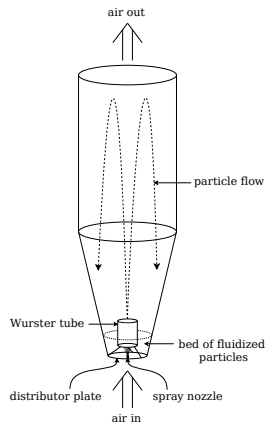

Figure 1.1: The Wurster type fluidised bed coating process.

The second application problem is related to quality control in material processing industries dealing with powders and granular materials. Granular media are commonly encountered in the pharmaceutical, food, agriculture, cement, and mineral processing industries as well as in combustion processes that use pulverised solid fuels. We focus on one particular aspect of quality control, namely the detection of anomalies such as the presence of undesirable objects in flowing granular materials. In this context, an undesirable object refers to a discrete solid item that somehow contaminates the material of interest. Undesirable objects may enter a process flow via raw materials, from fragments created when factory equipment break or due to sabotage or human mistakes by process operators. Such objects may cause damage and wear of process equipment or lead to malfunctioning end-products and even severe hazards to humans if a harmful object ends up in a food or pharmaceutical product. The conventional way to detect undesirable objects in the food and pharmaceutical industries is to use metal detectors and X-ray monitoring systems. However, these methods suffer from insufficient contrast and hence poor detectability for important classes of object materials including plastics, wood, and rubber. On the contrary, at microwave frequencies these materials may exhibit significant material contrast with respect to many relevant background media. Microwave-based detection systems may therefore be an important complement to existing techniques for detection of undesirable objects in industry. In Papers II-V, we present industrially viable measurement techniques based on microwave cavity resonator sensors with demonstrated capability to detect dielectric objects in flowing

granular materials.

This thesis consist of two parts, where the second part contains the appended publications. The first part serves to introduce the theory and methods upon which the research in the appended papers is based, and to motivate the choices of methods.

Chapter 2

MICROWAVE SENSING

The measurement problems studied in this thesis involve fluidised or flowing granular material mixtures that exhibit random fluctuations with respect to space and time. Our objective is to infer properties about these mixtures, such as the spatial variation of the density and moisture content or the presence of contaminating objects, based on microwave measurements. In the current chapter, we describe how microwave sensors can be designed and utilised in order to obtain the desired material properties. Furthermore, we review the electromagnetic theory and computational methods required to model the relationship between these material properties and the microwave sensor data.

2.1 Electromagnetic theory

The theory of classical electromagnetism, accomplished by J. C. Maxwell in the 1860's [2], describes the macroscopic interactions between electric charges in rest and in motion with outstanding accuracy. The interactions are commonly expressed via the electric and magnetic fields $\vec{E}$ and $\vec{H}$ and the flux densities $\vec{D}$ and $\vec{B}$, which are related to each other and to the sources $\vec{J}$ and ρ through Maxwell's equations [3]. Throughout this thesis, we assume that all fields exhibit harmonic time variation $e^{\mathrm{j}\omega t}$ and adopt a corresponding complex phasor representation. For this case, the time-harmonic Maxwell equations are given by

$$\nabla \times \vec{E} + \mathrm{j}\omega\vec{B} = \vec{0} \tag{2.1a}$$

$$\nabla \times \vec{H} - \mathrm{j}\omega\vec{D} = \vec{J} \tag{2.1b}$$

$$\nabla \cdot \vec{D} = \rho \tag{2.1c}$$

$$\nabla \cdot \vec{B} = 0. \tag{2.1d}$$

The fields and fluxes are related via the constitutive relations that involve the permittivity ϵ and permeability μ:

$$\vec{D} = \epsilon\vec{E} \tag{2.2a}$$

$$\vec{B} = \mu\vec{H}. \tag{2.2b}$$

By combining Eqs. (2.1) and (2.2), we obtain the vector Helmholtz wave equation

$$\nabla \times \left(\frac{1}{\mu}\nabla \times \vec{E}\right) - \omega^2\epsilon\vec{E} = -\mathrm{j}\omega\vec{J}. \tag{2.3}$$

For non-magnetic media where $\mu = \mu_0$, the propagation of electromagnetic waves is governed by the complex permittivity

$$\epsilon = \epsilon' - \mathrm{j}\epsilon'' = \epsilon_0(\epsilon'_\mathrm{r} - \mathrm{j}\epsilon''_\mathrm{r}) \tag{2.4}$$

where $\epsilon_\mathrm{r} = \epsilon'_\mathrm{r} - \mathrm{j}\epsilon''_\mathrm{r}$ is the relative permittivity or dielectric constant, and ϵ_0 is the permittivity of vacuum. The real part ϵ' describes the ability of the medium to store electric energy whereas the quantity ϵ'' accounts for processes in which electric energy is dissipated into heat. The latter may include conductive charge transport, so a material with non-zero conductivity σ can therefore be modelled by including the term σ/ω in ϵ'', if the frequency is non-zero. Given the time convention $e^{\mathrm{j}\omega t}$, a passive material must obey $\omega\mathrm{Im}\{\epsilon\} < 0$ and hence, given Eq. (2.4), $\epsilon'' > 0$ for positive frequencies. The losses in a material is commonly characterised by the loss tangent $\tan\delta = (\epsilon''/\epsilon')$. The origin to a material having a real permittivity $\epsilon' > \epsilon_0$ is the polarization (i.e. local charge separation) that is caused by an applied electric field. Depending on the constituent substances and the structure of the material, different polarisation mechanisms may occur such as electronic, molecular, orientational, and interfacial polarisation [3]. Each polarisation process may be associated with dissipative forces that give rise to a non-zero ϵ''. The response due to an applied electric field is generally not instantaneous but evolves on a certain time-scale, which implies that the induced polarisation and hence the permittivity depends on the frequency of the applied field, which is known as dispersion. The principle of causality, which states that the polarisation response cannot occur before the application of the field, implies that the functional behaviour of $\epsilon'(\omega)$ and $\epsilon''(\omega)$ must fulfil certain relationships which are known as the Kramers-Kronig relations [3]. Materials that contain molecules with a permanent dipole moment, such as water, typically exhibit orientational polarisation where the dipole moments may align with the applied electric field and thereby cause a strong net polarisation. If the external field vanishes, thermal molecular motion leads to a decay in the polarisation which, to a good approximation, follows a first-order step-response with a relaxation time τ. The dispersion of water and other polar substances in a condensed state can therefore be described by the Debye model [4]

$$\epsilon(\omega) = \epsilon_\infty + \frac{\epsilon_\mathrm{s} - \epsilon_\infty}{1 + \mathrm{j}\omega\tau}, \tag{2.5}$$

where ϵ_∞ and ϵ_s are the optical and static permittivities, respectively. Hence, $\epsilon' \approx \epsilon_\mathrm{s}$ at low frequencies and $\epsilon' \approx \epsilon_\infty$ at high frequencies, and the transition occurs around

the relaxation frequency, $\omega \approx 1/\tau$ where also the dielectric loss ϵ'' increases dramatically. For pure water at room temperature, $\epsilon'_{\mathrm{r}} \approx 80$ at frequencies below the relaxation frequency which occur approximately around 10 GHz.

A plane electromagnetic wave that propagates in the direction $\hat{k}$ has an electric and magnetic field that vary in space according to $e^{-\gamma \hat{k}\cdot\vec{r}}$, where $\gamma = \alpha + \mathrm{j}\beta$ is the propagation constant that must fulfil $\gamma^2 = -\omega^2\mu_0\epsilon$ for Eq. (2.3) to be satisfied. The attenuation factor α and the wave number β are then given by

$$\alpha = \frac{\omega}{\sqrt{2}}\sqrt{\mu_0\epsilon'\left(\sqrt{1+\left(\epsilon''/\epsilon'\right)^2}-1\right)} \tag{2.6}$$

$$\beta = \frac{\omega}{\sqrt{2}}\sqrt{\mu_0\epsilon'\left(\sqrt{1+\left(\epsilon''/\epsilon'\right)^2}+1\right)}. \tag{2.7}$$

As the name suggests, the attenuation factor α describes the attenuation of the wave's amplitude per unit propagation distance and it can be noticed from Eq. (2.6) that α increases with increasing dielectric losses ϵ''. The wave's group velocity is given by

$$v_{\mathrm{g}} = \frac{\partial\omega}{\partial\beta} = \left(\frac{\partial\beta}{\partial\omega}\right)^{-1}, \tag{2.8}$$

which, from Eq. (2.7), is seen to decrease as ϵ' increases (unless some special frequency dependence of $\epsilon(\omega)$ renders the opposite). Hence, the propagation delay is generally higher for a medium with higher real permittivity. In many microwave sensing applications, the parameters of interest to measure are related to the complex permittivity of the measurement object. Therefore, microwave sensors are commonly designed to measure changes in the delay and attenuation of microwaves that result from the interaction with the measurement object.

2.1.1 Homogenisation

Many materials of interest for microwave measurements are heterogeneous mixtures of different constituent materials. This is particularly true for the granular materials considered in this thesis, where solid dielectric particles, possibly together with fine dust and liquid droplets, are dispersed in a homogeneous host matrix, the air. The electromagnetic response of such mixtures can be modelled using an effective permittivity, defined through a volume-averaged constitutive relation according to

$$< \vec{D} >_{\vec{r}} = \epsilon_{\mathrm{eff}}(\vec{r}) < \vec{E} >_{\vec{r}}, \tag{2.9}$$

which applies at a certain point $\vec{r}$ in space. The volume average may be defined according to

$$< \vec{D} >_{\vec{r}} = \frac{1}{V_{\mathrm{c}}}\int_{V_{\mathrm{c}}} \vec{D}(\vec{r}\,')\mathrm{d}v', \tag{2.10}$$

for a control volume V_c centred at $\vec{r}$ that is large compared to the size of the inhomogeneities. Given the permittivity, the relative occurrence, and the geometry of the mixture components, the effective permittivity can be calculated using electromagnetic mixing formulas, a subject thoroughly covered in the book by Sihvola [5].

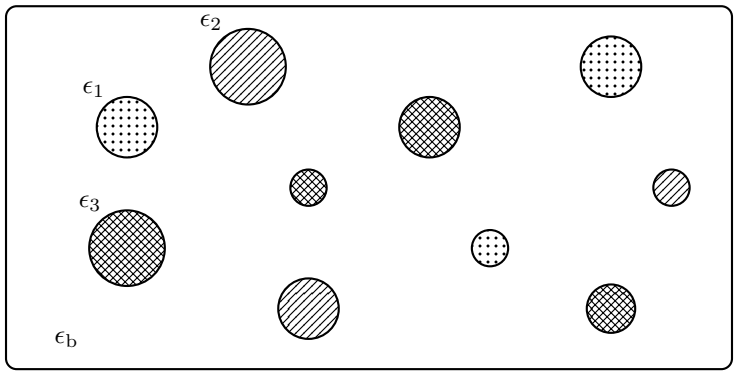

Figure 2.1: A multiphase mixture with spherical inclusions of different permittivities embedded in a homogeneous host matrix.

In this thesis, we limit our consideration to spherical inclusions that are randomly dispersed in a homogeneous background medium. By further assuming that the particles are small in comparison with the wavelength of the exciting field, the induced dipole moments of the inclusions (being the source to the macroscopic polarization) can be calculated under quasi-static assumptions where the applied field is approximated to be homogeneous in the vicinity of an inclusion. For a mixture composed of K different types of spherical inclusions embedded in a homogeneous background as depicted in Fig. 2.1, the well known Maxwell-Garnett model [6] predicts the following relation for the effective permittivity

$$\frac{\epsilon_{\text{eff}} - \epsilon_b}{\epsilon_{\text{eff}} + 2\epsilon_b} = \sum_{k=1}^{K} \nu_k \frac{\epsilon_k - \epsilon_b}{\epsilon_k + 2\epsilon_b} \tag{2.11}$$

where ν_k is the volume fraction for inclusions of type k. For dilute mixtures, i.e. where $\nu_k \ll 1$ for $k = 1, \ldots, K$, the effective permittivity according to Eq. (2.11) to the leading order in the volume fractions yields the intuitive result

$$\epsilon_{\text{eff}} \approx \epsilon_b + \sum_{k=1}^{K} n_k \alpha_k \tag{2.12}$$

where n_k is the number of inclusions of type k per unit volume and α_k is the polarizability of the inclusions [5]. It should be emphasized that the effective permittivity according to the Maxwell-Garnett model is independent of the particle size, as long as the quasi-static assumption is valid for the largest particles.

An important special case of Eq. (2.11) is the two-phase mixture ($K = 1$) with lossy and dispersive inclusions, which yield a complex and dispersive effective permittivity.

For instance, a Debye material in the inclusion phase yields a mixture that is also a Debye material, but the parameters in the Debye model, such as the relaxation frequency, varies with the mixing ratio [7]. Applying Eq. (2.11) with the inclusion permittivity $\epsilon_\mathrm{i} = \epsilon_\mathrm{i}' - \mathrm{j}\epsilon_\mathrm{i}''$ and a lossless background yields the complex effective permittivity

$$\epsilon_\mathrm{eff} = \epsilon_\mathrm{eff}' - \mathrm{j}\epsilon_\mathrm{eff}'' = \epsilon_\mathrm{b} + 3\nu\epsilon_\mathrm{b}\frac{\epsilon_\mathrm{i}' - \epsilon_\mathrm{b} - \mathrm{j}\epsilon_\mathrm{i}''}{\epsilon_\mathrm{i}' + 2\epsilon_\mathrm{b} - \nu(\epsilon_\mathrm{i} - \epsilon_\mathrm{b}) - \mathrm{j}\epsilon_\mathrm{i}''(1-\nu)}. \tag{2.13}$$

Given the dependence of ϵ_eff' and ϵ_eff'' on the volume fraction ν prescribed by Eq. (2.13), we may construct a function of ϵ_eff' and ϵ_eff'' that eliminates the dependence of ν and leaves us with something that only depends on the complex permittivity of the inclusions. Such *density-independent functions* are commonly used in microwave aquametry to obtain reliable moisture measurements of compressible materials when the density is unknown or varying [8]. For dilute mixtures with $\nu \ll 1$, it can be shown that both $\epsilon_\mathrm{eff}' - \epsilon_\mathrm{b}$ and ϵ_eff'' are proportional to ν. In this case, the ratio $\epsilon_\mathrm{eff}''/(\epsilon_\mathrm{eff}' - \epsilon_\mathrm{b})$ yields a density independent function that is commonly used in moisture measurements [9, 10]. At higher volume fractions and for more involved mixtures, other density-independent functions are required for decent elimination of the density dependence, and several candidate functions have been evaluated in the literature [11–13]. The best choice for a particular application, that minimises the influence of density over a range of measurement frequencies and moisture contents, is often selected based on experimental comparisons.

It should be mentioned that several mixing models apart from the Maxwell-Garnett rule have been proposed and are commonly used, including the Bruggeman and the Coherent potential formulas [14, 15]. For spherical inclusions with permittivity ϵ_i and volume fraction ν, all the mentioned models can be seen as special cases of the following unified model

$$\frac{\epsilon_\mathrm{eff} - \epsilon_\mathrm{b}}{\epsilon_\mathrm{eff} + 2\epsilon_\mathrm{b} + \xi(\epsilon_\mathrm{eff} - \epsilon_\mathrm{b})} = \nu\frac{\epsilon_\mathrm{i} - \epsilon_\mathrm{b}}{\epsilon_\mathrm{i} + 2\epsilon_\mathrm{b} + \xi(\epsilon_\mathrm{eff} - \epsilon_\mathrm{b})}. \tag{2.14}$$

Here, the Maxwell-Garnett rule is recovered by setting $\xi = 0$, whereas $\xi = 2$ yields the Bruggeman formula and $\xi = 3$ the Coherent potential formula [16]. For low volume fractions, all these formulas yield the same result, i.e. Eq. (2.12), but their predicted ϵ_eff differ at higher volume fractions, especially when the ratio $\epsilon_\mathrm{i}/\epsilon_\mathrm{b}$ is high [5].

Any mean-field theory that predicts a deterministic value for ϵ_eff for a random mixture will generally be incorrect for an arbitrary realisation of the mixture configuration. A reasonable approach to homogenisation is therefore to solve the field problem for many different specific realisations of the random mixture by a numerical method, and calculate the effective permittivity based on the volume-averaged field solutions. This approach, which yields a distribution of random effective permittivites, has been pursued in 2D by electrodynamic simulations using the finite-difference time-domain (FDTD) method [17, 18] and in 3D by static simulations [19]. In these works, it is found that the numerical results for ϵ_eff over the entire range of volume fractions tend to agree best with Eq. (2.14) for values of ξ between 0 and 2 (in 3D), i.e. somewhere between the Maxwell-Garnett and the Bruggeman formulas. Continued works on simulation-based prediction of the effective dielectric properties for heterogeneous mixtures are presented in [20–22].

2.1.2 Computational electromagnetics

The ability to solve electromagnetic field problems is central for the design and optimisation of microwave sensing devices and for interpretation of the resulting sensor data. Analytical solutions to Maxwell's equations, which can be obtained by the method of separation of variables, are available only in a limited number of special situations where the boundaries of the problem conform with some of the coordinate axes in a suitable coordinate system. In attempts to apply analytical methods also to problems of more practical interest, one or several approximations are typically made that limit the accuracy of the result. Therefore, numerical methods for solving Maxwell's equations using computers are invaluable tools for predicting the behaviour of wide classes of electromagnetic devices with high accuracy.

The field of computational electromagnetics (CEM) comprises methods for solving Maxwell's equations numerically, where the most prominent methods are the finite-difference time-domain (FDTD) method, the finite element method (FEM) and the method of moments (MoM) [23]. The two former methods are volume discretising methods, whereas the MoM is typically used with a discretisation only of the domain boundary. The FDTD method, proposed by Yee in 1966 [24], is very commonly used, partly due to its straight-forward implementation and computational efficiency for time-domain simulations that makes it particularly suitable for problems with wide-band excitation. However, the FDTD relies on a structured Cartesian grid to represent the fields, materials, and boundaries, which leads to inaccuracies for geometries that do not conform with the surfaces defined by a constant value for one of the Cartesian coordinates. The FEM employs unstructured meshes (e.g. tetrahedrons in 3D) that can approximate arbitrarily shaped boundaries with high accuracy and, in addition, such meshes allow for local refinement. The FEM yields implicit time-stepping in the time domain, which increases the computational effort as compared to the FDTD. However, the FEM is well suited for eigenvalue problems and driven problems with time-harmonic excitations [25]. The MoM is based on the integral formulation of Maxwell's equations in the frequency domain, and it typically uses the sources (i.e. currents or charges on the domain boundaries) as the unknown quantities rather than the fields. The sources are related to the fields via Green's functions and the information necessary to solve for the sources is obtained by requiring that the fields satisfy the appropriate boundary conditions. The MoM is well suited for free-space problems such as scattering problems and antenna analysis. However, it has severe inherent limitations for handling arbitrary inhomogeneous dielectrics, unless it is hybridised with a volume discretising method (such as the FEM) that accounts for the inhomogeneous part of the problem.

The electromagnetic field problems encountered in this thesis have certain aspects in common: (i) the computational domain is completely or partially enclosed by curved metal boundaries, (ii) inhomogeneous dielectrics are present, and (iii) we seek the solution at frequencies close to a number of distinct resonant frequencies. These aspects motivate our choice to use the FEM as the main computational method for the work contained in this thesis.

2.2 Microwave sensors

In the previous section it was concluded that, for non-magnetic materials, the propagation of microwaves is governed by the complex permittivity of the medium. By measuring the propagation effects using a microwave sensing device we can therefore attempt to estimate the complex permittivity, possibly including its spatial and temporal variation and frequency dependence. The permittivity may, in turn, be used to determine the physical properties of interest for the measurement object. The field of microwave sensing for industrial measurement problems is thoroughly covered in the book by Nyfors and Vainikainen [26]. Microwave sensors can be categorised based on their principle of operation, such as transmission, reflection, resonance, radiometric, and tomographic sensors. A brief description of the sensor types that are relevant to the measurement problems considered in this thesis, are presented in the following.

Transmission sensors

Transmission sensors are used to estimate the complex permittivity of a sample placed between two antennas or inside a waveguide, based on the attenuation and phase-shift caused by the sample. This method is both straight-forward and versatile, but requires that the shape of the sample (especially the thickness) is known or can be measured with other methods. For in-line process measurements, this typically requires that the material is transformed into a known shape, for example using a dielectric pipe. Furthermore, transmission measurements typically yield low accuracy in the determination of dielectric losses for low-loss materials.

Reflection sensors

Reflection sensors work by the principle to register the signal reflected from the measurement object. Typically, an open-ended transmission line or waveguide is put in contact with the measurement object and the complex reflection coefficient is measured as function of frequency. A common example is the open-ended coaxial probe that can be used to measure the complex permittivity of liquid and moldable materials that are put in contact with the probe. As the sensing volume is limited to that of the fringing fields at the probe tip, this technique has limited accuracy and requires good contact with the material to be measured, as well as careful calibration.

Radar sensors

A monostatic radar sensor, where the transmitting and receiving antennas are collocated, differs from a typical reflection sensor in that a variety of transmitted signal waveforms and receiver signal processing techniques may be employed to estimate the range, velocity, material, and geometry of the scattering object. Range and velocity information can be inferred from time-of-flight measurements for pulsed radars, or from the frequency-modulation of continuous-wave signals caused by moving objects due to the Doppler effect. Bi-static radars, where the transmitting and receiving antennas are

separated a considerable distance relative to the range of the object, can reveal more detailed information by measuring the scattered signal at different angles.

Imaging sensors

The aim of a microwave imaging sensor is to reconstruct an "image" in the form of a spatially varying permittivity, based on data from an antenna system that illuminates the measurement object and measures the scattered field at multiple directions. The reconstruction of the permittivity from the measured scattering data is, in general, a non-linear ill-posed inverse problem that can be very challenging to solve due to the complex scattering environment created by an inhomogeneous measurement object and the antenna system [27].

Resonator sensors

A microwave resonator is a device that, if excited, accumulates energy that continuously commutes between electric energy associated with charge separation and magnetic energy associated with currents. Resonator sensors are typically used by observing the changes in the resonator's oscillating frequency f_0 and quality factor Q that are caused by the interaction of the measurement object with the electric field. A resonator with high Q makes it possible to obtain very sensitive measurements also for small measurement objects with low permittivity and low losses. Furthermore, resonator sensors are more robust to instrument calibration errors than transmission or reflection sensors, which is beneficial for the long-term measurement stability. This is because it is the location and width of the resonant peak that determines f_0 and Q and not directly the absolute amplitude and phase of the transmission or reflection coefficient.

2.2.1 Applications

Although microwave sensing is a mature subject that has been used in industrial applications for more than 40 years, it is still an active field of research where new microwave measurement systems are continuously developed to target new applications and measurement problems. This section gives an overview (which is by no means exhaustive) of the reported applications of microwave sensors to various industrial and non-industrial measurement problems.

Microwave aquametry, i.e. the determination of moisture content based on permittivity measurements at microwave frequencies, is one of the most common microwave sensing applications, and a subject of its own [28]. Moisture content is an important property that affects the behaviour during processing and storage as well as the quality and trading value for many materials. Therefore, in-line moisture meters play a key role for process monitoring and quality control in many industries. Microwave sensors are used to measure the moisture content of agricultural products [29, 30], food [31], pharmaceutical substances [10, 32, 33], timber [34], paper [35], soil [36], and snow [37–39].

A common aim in the oil-and-gas industry is to monitor various properties of petroleum products. For instance, the measurement of water and gas fractions of oil mixtures flowing in pipes have been adressed using various resonator sensors [40, 41]. Also,

wide-band dielectric spectroscopy at microwave frequencies has been employed for in-line determination of the hydrocarbon composition in crude oil [42–44]. Furthermore, multiphase flow characterisation of petroleum flows in pipes has been addressed using microwave tomography [45, 46] and reflection measurements [47].

Transportation of powders and granular materials in pipes by means of pneumatic conveying is common in many industries. Microwave sensors have been applied in this setting to the measurement of particle size [48], particulate loading [49, 50], mass flow [51, 52], and flow inhomogeneities [53]. Related to the flow of particulate solids in gases is the field of gas sensing, where microwave sensors have been used to detect gaseous compounds such as ammonia [54], monitoring of combustion and exhaust fumes [55–57] and for detecting solid particulates in gas flows [58].

Microwaves can also be used to measure geometrical features such as distance, size, and movement of objects. Some examples on this topic include measurement of material levels in tanks and silos using radar [59], piston position and movement in combustion engines [55], and vibrations and movements in high-voltage power lines [60]. Related to this class of measurements is the fast growing field of automotive radars that are central for many active safety and driver assistance systems [61, 62].

Furthermore, microwave sensing has been applied to biology related applications such as plant growth monitoring [63], microfluidic sensing [64, 65] and in biomedical applications such as the diagnosis of stroke [66] and breast cancer [67].

2.3 Resonator sensors

In this thesis, resonator sensors are selected for the measurement problems at hand due to their high sensitivity and robustness. Resonant sensors can be realised in different ways, depending on the underlying resonant phenomena and the resonating structure. The most common types include (i) metal cavities, possibly with openings that allow for sample insertion; (ii) dielectric resonators, either put in contact with the sample or by using the sample itself as a dielectric resonator [68]; (iii) coplanar resonators based on e.g. microstrip lines where the strip can be shaped as rings, spirals or straight lines in order to comply with different sensing volume geometries and operating frequencies; (iv) transmission line resonators with two parallel conductors; (v) coaxial resonators, either with an open end put in contact with the sample or by filling the space between the conductors by the material to be measured; and (vi) open resonators where transverse electromagnetic (TEM) modes are operated between two conducting reflectors between which the sample is located.

2.3.1 Measurements using multiple resonant modes

The traditional way to perform resonator measurements is to use one single resonant mode whose resonant frequency and Q-value are used to determine the complex permittivity of a material sample [69]. Sometimes, one additional mode that is intentionally insensitive to the permittivity of the sample is used to compensate for disturbances caused by, e.g., thermal variations or dust deposition [26].

Although taking advantage of the high sensitivity and robustness achievable with resonators, a single-mode measurement yields no spatial information apart from a volume-averaged permittivity that is valid at a single frequency, i.e. the resonant frequency. Therefore, measurements that simultaneously employ multiple resonant modes open up for new possibilities enabled by the spatial diversity of the electromagnetic fields of the different modes, and the wide-band information obtained from multiple frequencies. Quite recently, a number of microwave measurement techniques that exploit multiple resonant modes have been presented, such as (i) wide band permittivity measurements using cavities, coaxial resonators and spiral-shaped microstrip resonators [54,70,71]; (ii) simultaneous dielectric and magnetic sensing of liquids [72]; (iii) characterisation of inhomogeneous cross-sectional flow profiles [73], and (iv) estimation of a spatially varying permittivity distribution in 3D using cavity resonances [74] (i.e. Paper I). To the best of the author's knowledge, there are few reported examples where multiple resonant modes are used to attempt to reconstruct a spatially varying permittivity. Fischerauer et al. considered this problem in the context of electrochemical process monitoring in vehicle catalysts and particulate filters by using the catalyst housing as a microwave cavity [56,57]. They observed diversity between different cavity modes to inhomogeneous permittivity perturbations and registered the microwave output of several resonances due to changes in the electrochemical state. However, they did not proceed to solve the inverse problem to estimate the spatially dependent permittivity perturbations from measured perturbations in the resonator parameters.

The measurement techniques presented in this thesis, described in Chapter 4 and in the appended papers, are all based on the principle to exploit the spatial diversity of multiple resonant modes for the estimation of a spatially varying permittivity or the detection of anomalies in granular flows.

2.4 Cavity resonators

The measurement techniques presented in this thesis are all based on resonant cavity sensors. As stated in Section 2.2, resonator sensors provide high sensitivity to small variations in the permittivity and are relatively stable to instrument calibration errors. Furthermore, cavities can provide volume-averaged permittivity measurements that yield global information from an entire material volume or the entire cross-section of a flow. In this section, we review the theory of microwave cavities including sensitivities to material and shape perturbations, and discuss practical aspects related to cavity design and the extraction of resonator parameters from measured scattering parameter (S-parameter) data.

A cavity resonator can be any hollow metal box that encloses a dielectric region of space. The solutions to Maxwell's equations inside closed cavities consist of a discrete set of resonant eigenmodes associated with a corresponding set of resonant frequencies. For waveguide cavities, which are formed by short-circuiting both ends of a waveguide with circular or non-circular cross-section, the eigenmodes can be classified as transverse electric (TE) and transverse magnetic (TM), characterised by a vanishing longitudinal electric and magnetic field component, respectively. Details related to the eigen-

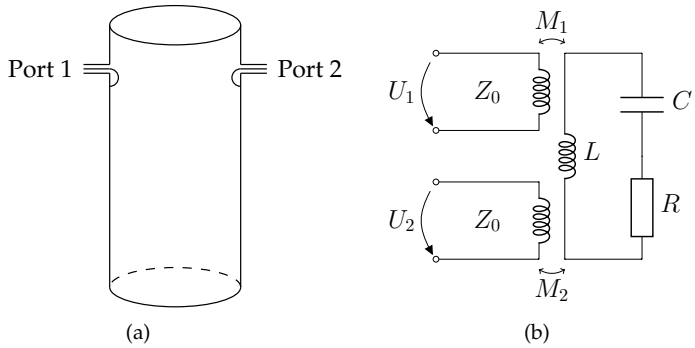

Figure 2.2: Electrical characteristics of a resonant cavity. (a) Cavity with two coupling loops. (b) Equivalent circuit model.

modes of rectangular and circular waveguide cavities can be found in e.g. [75] and [76].

Figure 2.2(a) shows a metal cavity that is closed except for two small coupling loops that are connected to transmission lines with impedance Z_0. If a sinusoidal voltage with frequency ω is applied at one of the ports, the induced voltage on the opposite port will be very low except at frequencies close to any of the cavity's resonant frequencies. At these frequencies, strong fields build up inside the cavity and the transmitted power between the ports increases dramatically. Close to a particular resonant frequency ω_0, the electromagnetic interaction between the probes can be modelled by the lumped circuit shown in Fig. 2.2(b) which has the resonant frequency $\omega_0 = (LC)^{-1/2}$ and the unloaded quality factor $Q_\mathrm{u} = 1/(\omega_0 RC) = \omega_0 L/R$. If we neglect any series resistance and self-inductance of the probes, the transmission coefficient can be calculated as

$$S_{21}(\omega) = \frac{U_2(\omega)}{U_1(\omega)} = \frac{K}{1 + \mathrm{j}Q\left(\frac{\omega}{\omega_0} - \frac{\omega_0}{\omega}\right)}, \tag{2.15}$$

where $K = 2\sqrt{\beta_1\beta_2}/(1 + \beta_1 + \beta_2)$, and $\beta_i = \frac{(\omega M_i)^2}{RZ_0}$ for $i = 1, 2$, are the coupling coefficients that depend on the size, position, and orientation of the probes via the mutual inductances M_1 and M_2 [77]. The radiation losses caused by the probes (which increase the effective series resistance in the resonant circuit model) lower the quality factor of the cavity, leading to a total, loaded quality factor given by

$$Q = Q_\mathrm{u}/(1 + \beta_1 + \beta_2). \tag{2.16}$$

The impedance seen from port 1 can be calculated as

$$Z(\omega) = Z_0 \frac{\beta_1}{1 + \beta_2 + \mathrm{j}Q_\mathrm{u}\left(\frac{\omega}{\omega_0} - \frac{\omega_0}{\omega}\right)} \tag{2.17}$$

which yields a reflection coefficient at port 1 given by

$$S_{11}(\omega) = \frac{Z(\omega) - Z_0}{Z(\omega) + Z_0} = \frac{\beta_1 - \beta_2 - 1 - \mathrm{j}Q_\mathrm{u}\xi}{\beta_1 + \beta_2 + 1 + \mathrm{j}Q_\mathrm{u}\xi} \tag{2.18}$$

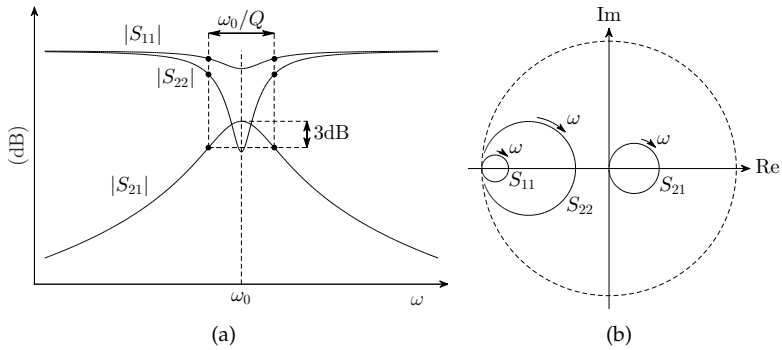

Figure 2.3: Transmission and reflection coefficients for the circuit model in Fig. 2.2(b) with coupling coefficients $\beta_1 = 0.2$ and $\beta_2 = 0.7$. (a) Magnitudes of S_{11}, S_{22} and S_{21} versus frequency, where the dots indicate frequencies at which the accepted and transmitted powers are half their maximum values; (b) locus of S_{11}, S_{22} and S_{21} in the complex plane together with the unit circle.

where $\xi = \omega/\omega_0 - \omega_0/\omega$. The corresponding expression for $S_{22}(\omega)$ is obtained analogously by swapping the positions of β_1 and β_2 in Eq. (2.18). Figure 2.3 shows the trace of $|S_{11}|$ and $|S_{21}|$ versus frequency, where the peaks are centred at ω_0 and has a half-power bandwidth given by ω_0/Q, and the locus of S_{11} and S_{21} in the complex plane.

Equations (2.15) and (2.18) describe the frequency domain response of a resonator subject to a forced excitation. In the time-domain, the fields of an excited resonance and thereby any output voltage signal, exhibit natural damped oscillations that persist for some time after the excitation has been removed. The time-variation of the fields can be expressed using a complex resonant frequency $\omega_\mathrm{c} = \omega_\mathrm{r} + \mathrm{j}\omega_\mathrm{i}$ according to

$$\vec{E}(\vec{r},t) = \mathrm{Re}\{\vec{E}_0(\vec{r})e^{\mathrm{j}\omega_\mathrm{c}t}\} = \mathrm{Re}\{\vec{E}_0(\vec{r})e^{\mathrm{j}\omega_\mathrm{r}t}\}e^{-\omega_\mathrm{i}t} \tag{2.19}$$

where the real part is the oscillating frequency and the imaginary part corresponds to the damping. The complex resonant frequency is obtained from the circuit model in Fig. 2.2(b) as the solution to $Z_\mathrm{r}(\omega_\mathrm{c}) = 0$, where

$$Z_\mathrm{r}(\omega) = R(1+\beta_1+\beta_2) + \mathrm{j}\left(\omega L - \frac{1}{\omega C}\right). \tag{2.20}$$

This is the equivalent impedance of the resonant circuit obtained by transferring the loading of both transmission lines to the resonant circuit side, which effectively increases the series resistance. The result is

$$\omega_\mathrm{c} = \mathrm{j}\frac{\omega_0}{2Q} \pm \omega_0\sqrt{1-\frac{1}{4Q^2}} = \mathrm{j}\omega_\mathrm{i} \pm \omega_\mathrm{r} \tag{2.21}$$

where $\omega_\mathrm{r} \approx \omega_0$ for lightly damped resonators. The stored energy $W(t)$ in the resonator, which is proportional to the squared magnitude of the field, then varies in time accord-

ing to

$$W(t) = W(0)e^{-(\omega_0/Q)t} \tag{2.22}$$

with a decay rate equal to the dissipated power $P(t) = -\dot{W}(t) = (\omega_0/Q)W(t)$. This motivates the common definition of Q as the ratio between the stored energy and the energy dissipated in one oscillation cycle times 2π:

$$Q = \omega_0 \frac{W}{P}. \tag{2.23}$$

2.4.1 Material and shape perturbations

The principle to measure material properties by observing the shift in the resonant frequency and Q-value of a cavity resulting from the insertion of a material sample is well known and dates back to the 1940's [78,79]. The resonant frequency is also perturbed by changes in the cavity's volume due to a boundary displacement or insertion of a metal object. The earliest treatments of the theory for material and shape perturbations were given by Bethe and Schwinger [80] and by Slater [81], respectively.

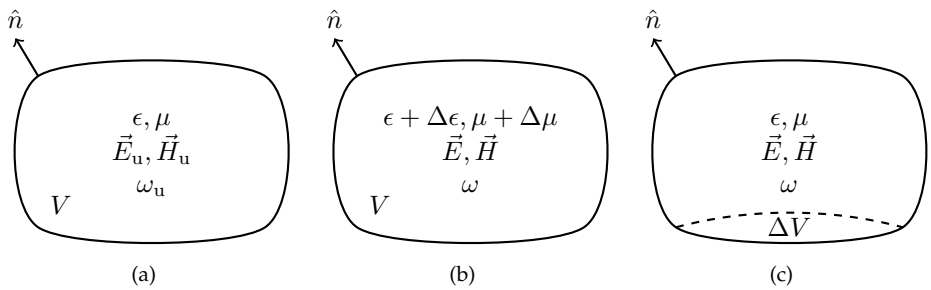

Figure 2.4: A closed metal cavity subject to material and shape perturbations. (a) Original unperturbed cavity; (b) cavity with perturbed material; (c) cavity with perturbed shape.

Consider a closed metal cavity that initially occupies an interior volume V with the loss-free permittivity ϵ and permeability μ as illustrated in Fig. 2.4(a). A certain eigenmode in this cavity has the fields $\vec{E}_\mathrm{u}$ and $\vec{H}_\mathrm{u}$ and resonant frequency ω_u which are assumed to be known. A material perturbation ($\Delta\epsilon$, $\Delta\mu$) that possibly introduces dielectric and magnetic losses, yields a change in the resonant frequency given by [82]

$$\frac{\omega - \omega_\mathrm{u}}{\omega} = -\frac{\int_V \left(\Delta\epsilon\vec{E}\cdot\vec{E}_\mathrm{u}^* + \Delta\mu\vec{H}\cdot\vec{H}_\mathrm{u}^*\right)\mathrm{d}v}{\int_V \left(\epsilon\vec{E}\cdot\vec{E}_\mathrm{u}^* + \mu\vec{H}\cdot\vec{H}_\mathrm{u}^*\right)\mathrm{d}v}. \tag{2.24}$$

If the perturbation is sufficiently small, the perturbed fields can be approximated by $\vec{E}_\mathrm{u}$

and $\vec{H}_{\mathrm{u}}$ and the resonant frequency by ω_{u}, which yields

$$\frac{\omega - \omega_{\mathrm{u}}}{\omega_{\mathrm{u}}} \approx -\frac{\int_V \left(\Delta\epsilon|\vec{E}_{\mathrm{u}}|^2 + \Delta\mu|\vec{H}_{\mathrm{u}}|^2\right) \mathrm{d}v}{\int_V \left(\epsilon|\vec{E}_{\mathrm{u}}|^2 + \mu|\vec{H}_{\mathrm{u}}|^2\right) \mathrm{d}v}. \tag{2.25}$$

Eq. (2.25) states that an increase in the permittivity at a location of nonzero electric field, or an increase in μ at a location of nonzero magnetic field, decreases the resonant frequency. By viewing ω, $\Delta\epsilon$ and $\Delta\mu$ as complex, it is also evident that a small increase in material losses yields a lower Q, via Eq. (2.21).

If a cavity perturbation measurement is used to accurately determine the complex permittivity of a sample with known shape, Eq. (2.24) should preferrably be used, which requires the perturbed fields inside the sample. If the sample is small compared to the wavelength, the unperturbed fields in the vicinity of the sample are approximately uniform and, consequently, the perturbed fields are governed by a quasi-static boundary value problem. For the special case of a dielectric ellipsoid in a homogeneous electric field aligned with any of the ellipsoid's axes, the static problem has an exact solution [83]. The ellipsoid result is very useful, since it yields as special cases the solution also for the sphere (three equal semi-axes) and the straight rod (one infinite semi-axis). Therefore, the permittivity can be estimated to a high accuracy for spherical and rod shaped samples by means of Eq. (2.24), also for materials whose permittivity deviates substantially from that of the unperturbed cavity. Several generalisations and extensions of the cavity perturbation method for improved accuracy and flexibility in terms of sample shape and permittivity range, have been reported [84–87], as well as accuracy analyses [88]. By exploiting numerical methods for electromagnetic field calculations, the cavity perturbation technique can be further extended to more general cavity and sample geometries [89, 90].

A cavity subject to a small boundary deformation as depicted in Fig. 2.4(c) yields a change in the resonant frequency that is given by Slater's theorem, which can be expressed according to

$$\frac{\omega - \omega_{\mathrm{u}}}{\omega_{\mathrm{u}}} \approx \frac{\int_{\Delta V} \left(\mu|\vec{H}_{\mathrm{u}}|^2 - \epsilon|\vec{E}_{\mathrm{u}}|^2\right) \mathrm{d}v}{\int_V \left(\mu|\vec{H}_{\mathrm{u}}|^2 + \epsilon|\vec{E}_{\mathrm{u}}|^2\right) \mathrm{d}v} \tag{2.26}$$

where the small volume ΔV has been removed from the unperturbed cavity [82]. This equation states that the resonant frequency increases if the cavity's boundary is moved inwards at a point of strong magnetic field (i.e. strong surface currents), whereas the resonant frequency decreases if the boundary is moved inwards at a point of strong electric field (i.e. high surface charge density). Eq. (2.26) is useful for cavity measurements aiming to monitor movements of the metal boundaries, and it specifies how a cavity can be tuned by the help of metal screws to change the resonant frequencies. Furthermore, Eq. (2.26) can be used to probe the fields inside a cavity by controlled positioning of a small metal bead, which is commonly done for cavities used in particle accelerators [91].

2.4.2 Cavity design considerations

When a cavity is used as a sensor for industrial measurements, several aspects need to be considered, including (i) the choice of resonant modes, (ii) the insertion of the measurement object or material, and (iii) the coupling to external circuitry. Although a cavity supports an infinite number of resonant modes, it is typically only a few of the low-order modes that can be reliably identified without risk for confusion with other modes and therefore are useful for sensing. It is clear from Eq. (2.25) that a resonant mode used for permittivity measurements should have an electric field maximum, or at least not a null, at the location of the sample.

Cavities used for industrial in-line measurements must necessarily allow for convenient insertion and removal of the measurement object or material to be measured, which prompts for holes or slot openings in the cavity wall. Holes should then be sufficiently small and slots should be oriented such that the perturbation to the surface currents are minimised, in order to reduce the radiation losses. If the material is a thin sheet, it is beneficial to use a circular-cylindrical cavity splitted in two halves operating in a TE_{01p} mode, whose electric field and surface currents are entirely azimuthal and thereby parallel to the opening. Another common solution for measuring dielectric rods or materials inside dielectric pipes is to use a circular-cylindrical cavity operating in the TM_{01p} mode, with holes in the top and bottom surface of the cavity where the sample is entered.

In order to excite resonant modes and to measure the resonator parameters, a cavity must be coupled to external microwave circuitry via transmission lines or waveguides. Two types of coupling devices that are commonly used together with coaxial transmission lines are E-probes and H-probes. An E-probe is formed by extending the inner conductor a short distance into the cavity, which then resembles a monopole antenna that couples to the normal component of the electric field of a resonant mode. The coupling is mainly determined by the length of the probe and the relative magnitude of the mode's electric field normal to the cavity wall at the probe location. An H-probe, or coupling loop, is formed by making a loop of the inner conductor that is short-circuited to the cavity wall and to the outer conductor. A current flowing in the loop yields a magnetic dipole moment directed normal to the loop surface, which may couple to an equally oriented magnetic field of the resonant mode. Cavities can also be excited from a waveguide through an aperture in the cavity wall, either via the tangential magnetic field or the normal electric field depending on the selected waveguide mode. The coupling is controlled by the size of the aperture and its location relative to the fields of the waveguide and cavity modes. The choice of coupling device is, among other things, affected by the physical environment in which the cavity operates. At very high temperatures that prevents the use of polytetrafluoroethylene (PTFE) insulated coaxial cables, aperture coupled all-metal waveguides is a suitable option. Furthermore, triboelectric charging of dielectric substances such as granulates [92], may impose high static voltages at the center conductor of an E-probe that can be harmful to the microwave instrumentation. More suitable in such situations are H-probes or waveguide apertures, which prevent high voltages of low frequency to reach the external circuitry.

2.4.3 Estimation of resonant frequency and quality factor

Resonator-based measurements usually require the resonant frequency $f_0 = \omega_0/(2\pi)$ and the unloaded quality factor Q_u to evaluate the properties of interest. Hence, there is a need for methods to accurately and reliably estimate f_0 and Q_u from measured S-parameter data. Given a resonant peak such as that shown in Fig. 2.3(a), it comes natural to identify f_0 as the location of the peak and the loaded Q from the bandwidth between the frequency points that yield half the maximum transmitted power. If complex S-parameter data is available at a range of frequency points around the resonance, more accurate estimates can be obtained by fitting a function of the form of Eq. (2.15) using all available data, from which f_0 and Q is obtained [93]. The unloaded quality factor is obtained from Eq. (2.16) for a cavity with two probes using the loaded Q and the coupling factors, which may be obtained from the measured S_{11} and S_{22} at the resonant frequency using Eq. (2.18).

The trace of any S-parameter follows approximately a circular path in the complex plane as the frequency is swept across a single resonance, which implies that the resonator parameters can be obtained by geometrical circle fitting [94]. Due to crosstalk and remaining transmission line delay following an imperfect calibration, the circle is displaced and rotated about the origin [95]. Consequently, an error-corrupted transmission coefficient can be modelled as a linear fractional transformation of a normalised frequency difference $\xi = 2(\omega - \omega_0)/\omega_0$ according to

$$S_{21} = \frac{a_1\xi + a_2}{a_3\xi + 1}. \tag{2.27}$$

The desired resonator parameters f_0 and Q_u are obtained from the coefficients a_1, a_2 and a_3, which can be estimated by a suitable fitting procedure [95, 96].

Another option is to view the resonator as a linear system and use system identification methods to estimate the poles and residues in a generic pole-series expansion of the system response:

$$S_{pq}(\omega) = \sum_m \frac{\alpha_m}{\omega - \omega_m}. \tag{2.28}$$

The complex resonant frequencies ω_m (i.e. the system poles) yield the resonant frequency and the loaded Q via Eq. (2.21), and the unloaded quality factor can be calculated using the coupling factors which are associated with the residues α_m. There are several methods for estimating the parameters in rational transfer function models in the form of Eq. (2.28) such as maximum-likelihood, least-squares and subspace-based methods [97, 98]. The subspace approach, which is employed to some extent in all of the Papers I-V, is an example of a high-resolution frequency estimation method that has shown to be very powerful and efficient for the estimation of complex resonant frequencies from S-parameter data, especially if several neighbouring resonances are present in the frequency band of interest.

2.5 Microwave instrumentation

A very versatile instrument for laboratory and industrial microwave measurements is the vector network analyser (VNA). A VNA calculates the complex S-parameters of a microwave network by measuring the magnitude and phase of the reflected and transmitted waves from the network using stepped-frequency sinusoidal radio-frequency (RF) signals and heterodyne receivers. VNA:s can achieve very high dynamic range and frequency precision which, together with automatic error-correction based on calibration measurements, enables very accurate measurements. However, laboratory-grade VNA:s that provide high measurement performance and flexibility are often bulky and expensive which prohibits their use in many cost-sensitive industrial, medical and consumer applications. Furthermore, the measurement speed of a conventional stepped-frequency VNA is limited by, among other things, the time required to sequentially tune the oscillators to each of the desired measurement frequencies, which may be prohibitive for measurements on systems that change rapidly in time. Recently, a different VNA architecture has been introduced that is based on wide-band stimulus signals and broad-band receivers to capture measurements over a wide frequency band simultaneously without relying on frequency-stepping [99]. This approach can shorten the time for wide-band S-parameter measurements significantly, although the speed is of course limited by the fundamental trade-off between measurement duration and accuracy.

Frequency tracking circuits can be used to monitor single mode microwave resonators. The resonator is then included in a feedback loop where the output frequency of a voltage controlled oscillator (VCO) is automatically tuned to the resonant frequency. The control voltage to the VCO can then be used as a measure of the resonant frequency [100]. The VCO can also be tuned to a frequency corresponding to a given power level (such as half the maximum transmitted power), which makes it possible to deduce the resonator bandwidth and hence the Q-value. Frequency tracking circuits typically have fast response times and can therefore be used to monitor fast phenomena where the resonant frequency changes quickly in time [52, 101].

A third type of microwave instrumentation use time-domain pulsed measurements, where the response of a microwave network to a wide-band pulsed excitation is registered in the time-domain. In order to resolve the pulses properly, the receiver must operate at a sampling rate exceeding twice the highest signal frequency of interest, from the Nyquist sampling theorem. Pulses containing energy at microwave frequencies therefore requires analogue-to-digital converters (ADC) with very high bandwidth, which is currently achieved by expensive components or low bit-resolution. One method for extending the bandwidth of time-domain systems beyond the bandwidth of the ADC is equivalent time sampling. In this method, several identical pulses are transmitted repeatedly, where the sampling instant is slightly delayed between subsequent pulses in order to capture the entire waveform [102].

Currently, a significant amount of research effort is spent on the development of low-cost and portable VNA solutions at different levels of circuit integration [46, 103–106]. To enable a lower unit cost, these solutions are often specialised towards specific applications and therefore have limited measurement flexibility as compared to general-purpose commercial VNA:s. There is little doubt that an increased availability of low-

cost VNA solutions will enable the deployment of microwave measurements in an increasing number of industrial, medical and consumer applications.

Chapter 3

ESTIMATION, DETECTION AND SIGNAL MODELLING

From a signal processing point of view, the two measurement problems considered in this thesis can be formulated as the problem to

1. Estimate a set of parameters from time-series of sensor data,
2. Decide whether or not a signal of interest is present in a given data set.

The first problem is clearly an example of parameter estimation, described by estimation theory. The second is a detection problem, which can be viewed as a special case of classification with two available classes. This chapter introduces the theory and methods concerned with parameter estimation and detection, and discusses special aspects that occur for our measurement applications. In particular, special emphasis is put on parametric models for signals and probability distributions used in the estimation and detection problems at hand.

In the following, we let $\mathbf{x} = [x_1, \ldots, x_N]^{\mathrm{T}} \in \mathbb{R}^N$ denote a vector in which all relevant data from a sensor measurement is collected. Hence, data associated with different channels, frequencies, spatial positions, time samples, or complex data are assumed to be vectorised into $\mathbf{x}$ in an appropriate manner.

3.1 Parameter estimation

The aim in many measurement situations is to assign values to a set of parameters based on measurement data with a random component. This type of inference can be viewed as an estimation problem. The topic of estimation theory is extensively covered in the book by Kay [107]. The data $\mathbf{x}$ is here viewed as a realisation of a multivariate stochastic variable $\mathbf{X}$ which has a certain probability density function (PDF, or density for short) denoted $p_{\mathbf{X}}(\mathbf{x}; \boldsymbol{\theta})$. In the following, we may omit the sub-index and use $p(\mathbf{x}; \boldsymbol{\theta})$ to denote the PDF of $\mathbf{X}$ if this is clear from the context. Here, $\boldsymbol{\theta} \in \mathbb{R}^p$ is a vector containing all

parameters needed to fully specify the distribution. If some parameters in $\boldsymbol{\theta}$ are not of direct interest but still required to obtain the appropriate form of the PDF, these are called *nuisance* parameters. An estimator is a function that maps a data realisation $\mathbf{x}$ onto an estimate $\hat{\boldsymbol{\theta}}$ of a "true" parameter vector $\boldsymbol{\theta}$. A consequence of the randomness of $\mathbf{x}$ is that $\hat{\boldsymbol{\theta}}$ is also a multivariate random variable. The performance of an estimator is natural to characterise in terms of the bias $\mathbf{b}$ (i.e. the systematic error) and the covariance matrix $\boldsymbol{\Sigma}_{\hat{\boldsymbol{\theta}}}$ (which quantifies the estimation uncertainty) of $\hat{\boldsymbol{\theta}}$ which are defined as

$$\mathbf{b} = E[\hat{\boldsymbol{\theta}} - \boldsymbol{\theta}] \tag{3.1}$$

$$\boldsymbol{\Sigma}_{\hat{\boldsymbol{\theta}}} = E[(\hat{\boldsymbol{\theta}} - E[\hat{\boldsymbol{\theta}}])(\hat{\boldsymbol{\theta}} - E[\hat{\boldsymbol{\theta}}])^{\mathrm{T}}]. \tag{3.2}$$

Here $E[\boldsymbol{\xi}]$ is the expected value and $\boldsymbol{\xi}^{\mathrm{T}}$ is the transpose of the vector or matrix $\boldsymbol{\xi}$. The mean-squared error (MSE) is given by

$$\mathrm{MSE}(\hat{\boldsymbol{\theta}}) = E[||\hat{\boldsymbol{\theta}} - \boldsymbol{\theta}||^2] = ||\mathbf{b}||^2 + \mathrm{Tr}\left(\boldsymbol{\Sigma}_{\hat{\boldsymbol{\theta}}}\right) \tag{3.3}$$

where $||\boldsymbol{\xi}||^2 = \boldsymbol{\xi}^{\mathrm{T}}\boldsymbol{\xi}$ is the squared Euclidean norm of the real vector $\boldsymbol{\xi}$ and $\mathrm{Tr}(\mathbf{A}) = \sum_i \mathbf{A}_{ii}$ is the trace of the matrix $\mathbf{A}$.

When designing an estimator, it is natural to simultaneously aim for zero bias and the least possible variance in the parameter estimates. The estimator that fulfils these criteria is called the minimum variance unbiased estimator (MVU), which is generally difficult to find or it may depend on the unknown parameters and is hence not realisable. For an unbiased estimator, the smallest possible variance is given by the Cramér-Rao lower bound (CRLB)

$$\mathrm{var}(\theta_i) \geq \left[\mathbf{I}^{-1}(\boldsymbol{\theta})\right]_{ii} \tag{3.4}$$

for $i = 1, \ldots, p$, provided that $p(\mathbf{x}; \boldsymbol{\theta})$ satisfies certain regularity conditions [107]. Here, $\mathbf{I}(\boldsymbol{\theta})$ is the Fisher information matrix whose entries are given by

$$[\mathbf{I}(\boldsymbol{\theta})]_{ij} = -E\left[\frac{\partial^2 \ln p(\mathbf{x}; \boldsymbol{\theta})}{\partial\theta_i \partial\theta_j}\right]. \tag{3.5}$$

The CRLB can be intuitively understood by considering the single-parameter case where Eq. (3.5) is the log-likelihood function's expected curvature with respect to a single parameter θ. A larger curvature implies that the distribution of the parameter's value is more concentrated around its mean, which makes it possible to estimate it with smaller uncertainty. An unbiased estimator that attains the Cramér-Rao bound is said to be efficient and, hence, it is the MVU estimator. A powerful remedy in situations when the MVU cannot be practically realised is the maximum-likelihood estimator (MLE) which can be formulated according to

$$\hat{\boldsymbol{\theta}}_{\mathrm{MLE}} = \arg\max_{\boldsymbol{\theta}} L(\boldsymbol{\theta}|\mathbf{x}). \tag{3.6}$$

Here, $L(\boldsymbol{\theta}|\mathbf{x}) = p(\mathbf{x}|\boldsymbol{\theta})$ is the likelihood function which is the PDF viewed as a function of the parameters, conditioned on the observed data. The MLE is asymptotically

efficient for large data records. Furthermore, it can always be realised (at least in principle), although its implementation may involve a non-linear maximisation that can be challenging if the number of parameters is large. We employ the maximum-likelihood method in Papers III-V for estimating parameters in signal models that are used in detection algorithms. Another important estimation method is least-squares (LS), where the parameter estimate is obtained by minimising the squared Euclidean distance between a parameter-dependent signal model and the observed data according to

$$\hat{\boldsymbol{\theta}}_{\mathrm{LS}} = \arg\min_{\boldsymbol{\theta}} ||\mathbf{s}(\boldsymbol{\theta}) - \mathbf{x}||_2^2. \tag{3.7}$$

In this case, no assumptions regarding the statistical distribution of the data are required which makes the method straight-forward to implement for many different applications, although no optimality can be claimed in general. However, the least-squares estimator becomes efficient in the special case where the signal model is linear in the parameters and the noise in $\mathbf{x}$ is additive, white, and Gaussian distributed [107]. The least-squares method is employed in Paper I for the estimation of parameters that describe a spatially varying permittivity in 3D, based on measured resonant frequencies and temperature data.

In a frequentistic approach to estimation, $\boldsymbol{\theta}$ is viewed as deterministic vector whose value is inferred entirely based on data and the assumed signal model. This is the viewpoint maintained so far in this section. On the contrary, in the Bayesian approach, $\boldsymbol{\theta}$ is viewed as a random variable that has a certain probability distribution prior to the observation of any data, described by the prior density $p(\boldsymbol{\theta})$. After the data $\mathbf{x}$ has been observed, the probability distribution of $\boldsymbol{\theta}$ changes, and its posterior density $p(\boldsymbol{\theta}|\mathbf{x})$ is given by Bayes formula [107]

$$p(\boldsymbol{\theta}|\mathbf{x}) = \frac{p(\mathbf{x}|\boldsymbol{\theta})p(\boldsymbol{\theta})}{p(\mathbf{x})}. \tag{3.8}$$

Hence, the posterior density is proportional to the product of the likelihood function $p(\mathbf{x}|\boldsymbol{\theta})$ and the prior density. The point estimate $\hat{\boldsymbol{\theta}}$ can be obtained, for instance, from the mean or maximum of the posterior density, where the former yields the minimum mean-squared error (MMSE) estimator and the latter the maximum a posteriori (MAP) estimator:

$$\hat{\boldsymbol{\theta}}_{\mathrm{MMSE}} = E[\boldsymbol{\theta}|\mathbf{x}] = \int \boldsymbol{\theta} p(\boldsymbol{\theta}|\mathbf{x}) \mathrm{d}\boldsymbol{\theta}, \tag{3.9}$$

$$\hat{\boldsymbol{\theta}}_{\mathrm{MAP}} = \arg\max_{\boldsymbol{\theta}} p(\boldsymbol{\theta}|\mathbf{x}). \tag{3.10}$$

The MMSE and MAP point estimates coincide if the posterior density is symmetric, which is the case for Gaussian distributions. The Bayesian approach is appropriate when some information about the parameters to be estimated is available beforehand, in which case the variance and robustness to outliers in the data can be improved as compared to the frequentistic approach. However, Bayesian estimation introduces a risk for biasing the estimate towards a potentially incorrect prior distribution.

3.2 Signal detection

Detection theory deals with the problem to make a decision whether or not an event of interest has occurred based on a given data set. This problem finds applications in the detection of aircraft, boats and vehicles using radar or sonar, detection of symbols sent over a communication channel, detection of physiological disease states based on biomedical signals, detection of objects in images, and detection of faults or anomalies in machines and industrial processes. In this thesis, we consider the detection of undesirable objects in a flowing granular material based on microwave sensor data.

An important special case is the binary problem to detect if a signal of interest is present in noisy data, or if the data consist of noise only. Since there are only two available options, this is an example of a binary hypothesis test and of a binary classification problem. If we denote the noise-only option as the null-hypothesis $\mathcal{H}$ and the option of having a signal present as the alternative hypothesis $\mathcal{K}$, a hypothesis test can be formulated according to

$$\begin{aligned} \mathcal{H}: &\quad \mathbf{x} = \mathbf{w} \\ \mathcal{K}: &\quad \mathbf{x} = \mathbf{s} + \mathbf{w} \end{aligned} \tag{3.11}$$

where $\mathbf{x} \in \mathbb{R}^N$ is the observed data, $\mathbf{w}$ is the noise and $\mathbf{s}$ is the signal of interest. The detector can be expressed in terms of a discriminating function $T(\mathbf{x})$ that maps available data onto a real-valued scalar that determines which hypothesis to choose upon comparison with a threshold:

$$T(\mathbf{x}) \underset{\mathcal{H}}{\overset{\mathcal{K}}{\gtrless}} \eta. \tag{3.12}$$

This means that we accept $\mathcal{K}$ (i.e. decide for a positive detect) if $T(\mathbf{x}) \geq \eta$ and otherwise accept $\mathcal{H}$ if $T(\mathbf{x}) < 0$. The condition (3.12) partitions the data space $\mathbb{R}^N$ in two regions $\mathcal{R}_\mathcal{K} = \{\mathbf{x}\colon\ T(\mathbf{x}) \geq \eta\}$ and $\mathcal{R}_\mathcal{H} = \{\mathbf{x}\colon\ T(\mathbf{x}) < \eta\}$ such that $\mathcal{R}_\mathcal{K} \cup \mathcal{R}_\mathcal{H} = \mathbb{R}^N$ and $\mathcal{R}_\mathcal{K} \cap \mathcal{R}_\mathcal{H} = \emptyset$. The probabilities for detection and false-alarm as functions of the threshold can be expressed either from the PDF $p_\mathbf{X}(\mathbf{x})$ of $\mathbf{x}$ or the PDF $p_T(T')$ of $T(\mathbf{x})$ under each hypothesis according to

$$P_\mathrm{D}(\eta) = \int_{\mathbf{x}\in\mathcal{R}_\mathcal{K}} p_\mathbf{X}(\mathbf{x}|\mathcal{K})d\mathbf{x} = \int_\eta^\infty p_T(T'|\mathcal{K})dT' \tag{3.13}$$

$$P_\mathrm{FA}(\eta) = \int_{\mathbf{x}\in\mathcal{R}_\mathcal{K}} p_\mathbf{X}(\mathbf{x}|\mathcal{H})d\mathbf{x} = \int_\eta^\infty p_T(T'|\mathcal{H})dT'. \tag{3.14}$$

The performance of a detector is commonly characterised by a curve known as the receiver operating characteristic (ROC), where P_D is plotted versus P_FA for all values of the threshold η, which provides a graphical illustration of the trade-off between detection accuracy and false-alarm rate. Furthermore, the area under the ROC curve (AUC for short) is a summary statistic that characterises the overall classification performance,

where $\mathrm{AUC} = 1$ corresponds to perfect classification and $\mathrm{AUC} = 0.5$ corresponds to random guessing. Furthermore, the AUC has the important statistical interpretation as the probability that the the discriminating function $T(\mathbf{x})$ attains a higher value for a random instance where $\mathcal{K}$ is indeed true, than for a random instance where $\mathcal{H}$ is true [108], i.e.

$$\mathrm{AUC} = \Pr(T(\mathbf{x}|\mathcal{K}) > T(\mathbf{x}|\mathcal{H})). \tag{3.15}$$

If $p(\mathbf{x}|\mathcal{K})$ and $p(\mathbf{x}|\mathcal{H})$ are completely known, the Neyman-Pearson theorem states that the most powerful test, which maximises P_{D} subject to any fixed false-alarm constraint $P_{\mathrm{FA}} = \alpha$ is the likelihood ratio test (LRT) where the test statistic is given by the likelihood ratio or, equivalently, its logarithm [109]:

$$T_{\mathrm{LRT}}(\mathbf{x}) = \log\left(\frac{p(\mathbf{x}|\mathcal{K})}{p(\mathbf{x}|\mathcal{H})}\right). \tag{3.16}$$

If the signal $\mathbf{s}$ and the statistics of the noise $\mathbf{w}$ are not completely known but can be parametrised by the parameter vectors $\boldsymbol{\theta}_{\mathcal{H}}$ and $\boldsymbol{\theta}_{\mathcal{K}}$ under each hypothesis, a reasonable approach is to compute the maximum-likelihood estimates $\hat{\boldsymbol{\theta}}_{\mathcal{H}} = \mathrm{MLE}\,(\boldsymbol{\theta}_{\mathcal{H}}) = \arg\max_{\boldsymbol{\theta}_{\mathcal{H}}} p(\mathbf{x}|\mathcal{H};\boldsymbol{\theta}_{\mathcal{H}})$, and $\hat{\boldsymbol{\theta}}_{\mathcal{K}} = \mathrm{MLE}\,(\boldsymbol{\theta}_{\mathcal{K}})$, from data and insert the results into the log-likelihood ratio:

$$T_{\mathrm{GLRT}}(\mathbf{x}) = \log\left(\frac{p(\mathbf{x}|\mathcal{K};\hat{\boldsymbol{\theta}}_{\mathcal{K}})}{p(\mathbf{x}|\mathcal{H};\hat{\boldsymbol{\theta}}_{\mathcal{H}})}\right). \tag{3.17}$$

This is known as the generalised likelihood ratio test (GLRT) which often works well but lacks general optimality [107].

In a Bayesian approach to detection, prior information regarding the relative occurrence of $\mathcal{H}$ and $\mathcal{K}$ is incorporated in a detector that seeks to minimise the probability for making wrong decisions, or an associated cost [109]. In applications where it is difficult to estimate the likelihood to encounter a real target event (in our case the presence of a contaminating object), the frequentistic Neyman-Pearson approach is usually preferred over the Bayesian one. For this reason, we choose the Neyman-Pearson approach throughout the thesis.

For the case of a known deterministic signal $\mathbf{s}$ in zero-mean Gaussian distributed noise $\mathbf{w} \sim \mathcal{N}(\mathbf{0}, \boldsymbol{\Sigma})$ with known covariance matrix $\boldsymbol{\Sigma} = E[\mathbf{w}\mathbf{w}^{\mathrm{T}}]$, the LRT takes the form of a matched filter where the test statistic (i.e. the data-dependent part of the log-likelihood ratio) is given by

$$T(\mathbf{x}) = \mathbf{x}^{\mathrm{T}}\boldsymbol{\Sigma}^{-1}\mathbf{s}. \tag{3.18}$$

This discriminating function is linear in the data. Hence, in the context of classification, the matched filter detector is an example of linear discriminant analysis (LDA) where the data space is partitioned by a hyperplane defined by the weight vector $\boldsymbol{\Sigma}^{-1}\mathbf{s}$ [110]. If the signal is unknown but can be represented by a linear model according to $\mathbf{s} = \mathbf{H}\boldsymbol{\theta}$, where $\mathbf{H} \in \mathbb{R}^{N\times p}$ is a known observation matrix, the maximum-likelihood estimate of the signal is given by

$$\hat{\mathbf{s}} = \mathbf{H}\hat{\boldsymbol{\theta}} = \underbrace{\mathbf{H}(\mathbf{H}^{\mathrm{T}}\boldsymbol{\Sigma}^{-1}\mathbf{H})^{-1}\mathbf{H}^{\mathrm{T}}\boldsymbol{\Sigma}^{-1}}_{=\mathbf{P}}\mathbf{x} = \mathbf{P}\mathbf{x}. \tag{3.19}$$

Here, $\mathbf{P}$ is a rank-p projection matrix that projects onto the subspace of $\mathbb{R}^N$ spanned by the columns of $\mathbf{H}$. The resulting GLRT test statistic is given by

$$T(\mathbf{x}) = \mathbf{x}^{\mathrm{T}}\hat{\boldsymbol{\Sigma}}^{-1}\hat{\mathbf{s}} - \frac{1}{2}\hat{\mathbf{s}}^{\mathrm{T}}\hat{\boldsymbol{\Sigma}}^{-1}\hat{\mathbf{s}} = \frac{1}{2}\hat{\mathbf{s}}^{\mathrm{T}}\boldsymbol{\Sigma}^{-1}\hat{\mathbf{s}} \tag{3.20}$$

where the latter equality is obtained from the relations $\hat{\mathbf{s}} = \mathbf{P}\mathbf{x}$ and $\mathbf{P}^{\mathrm{T}}\boldsymbol{\Sigma}^{-1}\mathbf{P} = \boldsymbol{\Sigma}^{-1}\mathbf{P}$. The detector with the test statistic in Eq. (3.20) is known as an incoherent matched filter, and it is an example of quadratic discriminant analysis (QDA) since the discriminant function is quadratic in the data. By further considering the eigenvalue factorisation $\boldsymbol{\Sigma} = \mathbf{Q}\boldsymbol{\Lambda}\mathbf{Q}^{\mathrm{T}}$ where $\boldsymbol{\Lambda} = \mathrm{diag}(\lambda_1, \ldots, \lambda_N)$, $\mathbf{Q}_{\cdot,i} = \mathbf{v}_i$, and $\boldsymbol{\Sigma}\mathbf{v}_i = \lambda_i\mathbf{v}_i$, $i = 1, \ldots, N$, we can rewrite Eq. (3.20) as

$$T(\mathbf{x}) = \frac{1}{2}(\mathbf{Q}^{\mathrm{T}}\hat{\mathbf{s}})^{\mathrm{T}}\boldsymbol{\Lambda}^{-1}\mathbf{Q}^{\mathrm{T}}\hat{\mathbf{s}} = \frac{1}{2}\mathbf{y}^{\mathrm{T}}\boldsymbol{\Lambda}^{-1}\mathbf{y} = \frac{1}{2}\sum_{i=1}^{N}\frac{y_i^2}{\lambda_i} \tag{3.21}$$

where $\mathbf{y} = \mathbf{Q}^{\mathrm{T}}\hat{\mathbf{s}} = \mathbf{Q}^{\mathrm{T}}\mathbf{P}\mathbf{x}$. Hence, the component $y_i = \mathbf{v}_i^{\mathrm{T}}\mathbf{P}\mathbf{x}$ is the projection of the data on the signal subspace, in turn projected onto the noise eigenvector $\mathbf{v}_i$. The test static therefore attains a high value if $\mathbf{P}\mathbf{x}$ has a large component in the directions $\mathbf{v}_i$ in which the noise is weak and thus are associated with small λ_i. The incoherent matched filter is therefore very sensitive to data containing signals that lie in a subspace in which the noise is weak, and it attains perfect classification if the noise resides in a subspace of $\mathbb{R}^N$ (corresponding to some λ_i being zero) that is orthogonal to the signal subspace.

If the dimensionality p of the expected signal subspace is increased by adding columns to the observation matrix $\mathbf{H}$, the discriminative power of the matched filter is typically reduced as p increases. For $p = N$, the projection matrix becomes a full-rank matrix that maps any $\mathbf{x} \in \mathbb{R}^N$ onto itself, i.e. $\mathbf{P}\mathbf{x} = \mathbf{x}$. Equation (3.20) then reduces to the following quadratic function in $\mathbf{x}$

$$T(\mathbf{x}) = \frac{1}{2}\mathbf{x}^{\mathrm{T}}\boldsymbol{\Sigma}^{-1}\mathbf{x}, \tag{3.22}$$

which can be viewed as the power of the noise-whitened data $\boldsymbol{\Sigma}^{-1/2}\mathbf{x}$. Hence, no special information regarding the target signal is incorporated, which avoids the problem how to model $\mathbf{s}$. However, this approach will give poorer detection performance as compared to a matched filter that employs the correct signal model.

3.3 Random processes

A random process is a collection of random variables, each associated with a point in an underlying index set according to $\{X_t : t \in T\}$. The index set T commonly represents continuous or discrete time, leading to a continuous or discrete time stochastic process, respectively. The index set may also, for instance, be points in $\mathbb{R}^N$ that correspond to physical coordinates in an N-dimensional Euclidean space and, in this case, the stochastic process is referred to as a random field. For a fixed $t \in T$, the random

variable X_t maps a sample space Ω to a state space S, where $S = \mathbb{R}$ if the random variable X_t is continuous and real-valued. Furthermore, for a fixed $\omega \in \Omega$, the collection $\{x(t) = X_t(\omega), t \in T\}$ is called a realisation of the process [111].

If the random variable X_t is continuous and if its PDF $p_{X_t}(x)$ exists, the ensemble mean of the process is defined according to

$$m_x(t) = E[X_t] = \int_{-\infty}^{\infty} x p_{X_t}(x) dx, \tag{3.23}$$

where the expectation is taken with respect to all possible realisations. Furthermore, if we adopt the nomenclature commonly employed in signal processing literature [112], the *autocorrelation* function of a real-valued process is defined as

$$r_x(s,t) = E[X_s X_t] = \mathrm{cov}(X_s, X_t) + m_x(s) m_x(t). \tag{3.24}$$

The process X_t is said to be wide-sense stationary (WSS) if its mean is independent of t, i.e. $m_x(t) = m$, and the autocorrelation only depends on the lag $\tau = t - s$ but not the absolute time t according to $r_x(s,t) = r_x(t-s) = r_x(\tau)$. In addition, the process is strictly stationary if the joint distribution of the collection $\{X_{t_1}, \ldots, X_{t_N}\}$ for any $t_1, \ldots, t_N \in T$, is invariant under an arbitrary time-shift. Furthermore, a WSS process X_t is said to be ergodic (in the first two moments) if the mean and autocorrelation can be estimated to arbitrary accuracy from observations of one single realisation $\{x[n]\}_{n=0}^{N-1}$ of sufficiently long duration. Here, $x[n] = x(nT_\mathrm{s})$ denotes the discrete-time samples of a continuous-time process where T_s is the sampling interval. If we consider the following sample mean and sample autocorrelation estimates, the ergodicity can be expressed according to

$$\hat{m}_x = \frac{1}{N} \sum_{n=0}^{N-1} x[n] \to m \quad \text{as } N \to \infty \tag{3.25}$$

$$\hat{r}_x[l] = \frac{1}{N} \sum_{n=0}^{N-1-l} x[n] x[n+l] \to r[l] \quad \text{as } N \to \infty. \tag{3.26}$$

The power spectral density (PSD, also called power spectrum, or spectrum for short) describes how the power of a random process is distributed with respect to frequency. For a WSS discrete-time random process, the PSD can be defined as the discrete-time Fourier transform (DTFT) of the autocorrelation sequence [113] according to

$$P_x(\Omega) = \sum_{l=-\infty}^{\infty} r_x[l] e^{-\mathrm{j}\Omega l}. \tag{3.27}$$

Here, $\Omega = \omega T_\mathrm{s}$ is the normalised frequency (rad/sample) where ω is the physical frequency (rad/s). If a WSS discrete-time random process $x[n]$ is applied as the input to a stable, linear, and time-invariant system with impulse response coefficients $\{h[k]\}_{k=-\infty}^{\infty}$ then the output

$$y[n] = \sum_{k=-\infty}^{\infty} h[k] x[n-k] \tag{3.28}$$

is also a WSS random process. The PSD for $y[n]$ and $x[n]$ are related according to

$$P_y(\Omega) = |H(\Omega)|^2 P_x(\Omega). \tag{3.29}$$

Here, $H(\Omega)$ is the DTFT of $h[k]$ which is obtained by evaluating the transfer function $H(z)$ on the unit circle according to $z = e^{\mathrm{j}\Omega}$ for $\Omega \in [-\pi, \pi]$.

The concept of random processes is a useful tool for modelling sensor data that contain random components (correlated or uncorrelated) where the data is collected on an underlying temporal or spatial grid. In Paper II, we employ random processes in 3D to generate data that models a spatially varying stochastic permittivity for evaluating detection performance using a finite-element model. Furthermore, in Paper V, we use stochastic processes to model the spatial and temporal variation of the permittivity of flowing granular materials. Specifically, we use the relation (3.29) to estimate the power spectrum of a random permittivity (i.e. the input process to a linear system that models our sensor), based on the power spectrum of the measured microwave signals (the output process).

3.3.1 Gaussian processes

One class of random processes of particular usefulness are Gaussian processes, which are characterised by that the random variables X_t are normal distributed. Hence, the real-valued continuous-time random process X_t is a Gaussian process if each finite-dimensional vector $\mathbf{X} = [X_{t_1}, \ldots, X_{t_N}]^{\mathrm{T}}$ evaluated at the points $\mathbf{t} = [t_1, \ldots, t_N]^{\mathrm{T}}$ has a multivariate normal distribution [111] according to $\mathbf{X} \sim \mathcal{N}(\boldsymbol{\mu}, \boldsymbol{\Sigma})$ with the PDF given by

$$p_{\mathbf{X}}(\mathbf{x}; \boldsymbol{\mu}, \boldsymbol{\Sigma}) = \frac{1}{\sqrt{(2\pi)^N \det(\boldsymbol{\Sigma})}} \exp\left(-\frac{1}{2}(\mathbf{x} - \boldsymbol{\mu})^{\mathrm{T}} \boldsymbol{\Sigma}^{-1} (\mathbf{x} - \boldsymbol{\mu})\right). \tag{3.30}$$

Furthermore, the process is wide-sense stationary if the mean vector $\boldsymbol{\mu}$ and the covariance matrix $\boldsymbol{\Sigma}$ are invariant under a time-shift $\mathbf{t} \to \mathbf{t} + h\mathbf{1}_N$ for any real $h > 0$ where $\mathbf{1}_N = [1, \ldots, 1]^{\mathrm{T}} \in \mathbb{R}^N$. Since a normal distribution is entirely specified by its first two moments, a Gaussian process that is wide-sense stationary is consequently also strictly stationary.

The assumption of Gaussian statistics can often simplify the analytical manipulations involved in many estimation and detection problems, which allows for closed-form solutions to many problems of practical interest. Furthermore, many real-world stochastic phenomena can be accurately modelled by Gaussian distributions. This is explained by the central limit theorem, which states that the sum (and the average) of many independent random variables is asymptotically normal distributed. For instance, the thermal voltage noise across a resistor is well known to follow a Gaussian distribution, which is reasonable if the total voltage is viewed as the series connection of many small voltage contributions, each arising from random microscopic charge displacements. Another important example in the context of this thesis is a cavity resonator that is partly filled with a granular material mixture where the particle density fluctuates randomly with respect to space and time. Hence, the permittivity can be modelled

as a random process that is associated simultaneously with a spatial and temporal index set. By considering the material perturbation formula (2.25), we notice that the resonant frequency can be viewed as a weighted sum (or integral) of the permittivity variations at different points in space. It is therefore reasonable to expect that the resonant frequencies are approximately Gaussian distributed if the fluctuations in the material density, and hence in the effective permittivity, are sufficiently uncorrelated and small in comparison with the wavelength of the electromagnetic field. This fact is experimentally observed for the cavity containing a fluidised bed in Paper I, and the cavity sensors used to observe flowing granular materials in Papers III-V. As stated previously, a well-founded assumption of Gaussian distributed data enables or simplifies the derivation of optimal parameter estimation and detection algorithms. In measurement situations where the measured quantities are S-parameters, it is therefore an adequate approach to somehow map the S-parameters to a new set of data that corresponds to the complex resonant frequencies of the system, or a linear function thereof. Depending on the quality and the nature of the S-parameter data, this mapping can be accomplished in different ways and Section 4.3 summarises the approaches to this mapping problem that we use in Papers I-V.

3.3.2 Complex Gaussian distribution

Complex-valued data with a random component is commonly encountered in electrical engineering, hence it is useful to assign probability distributions to complex-valued vectors of random variables. Complex data arises naturally in the representation of a narrow-band signal $x(t)$ by its complex base-band signal $x_{\mathrm{B}}(t)$ according to

$$x(t) = \mathrm{Re}\{x_{\mathrm{B}}(t)e^{\mathrm{j}\omega_c t}\}. \tag{3.31}$$

where the spectrum of $x(t)$ is nonzero only in a narrow frequency band around the carrier frequency ω_{c} (and $-\omega_c$). Here, $x_{\mathrm{B}}(t) = I(t)+\mathrm{j}Q(t)$ where I and Q are the in-phase and quadrature signal components. This complex signal representation is encountered for narrow-band radio-frequency signals as well as in the context of harmonic circuit analysis. Complex data arises also in the frequency-domain representation of a real-valued signal if the Fourier transform is expressed using complex exponentials.

For a complex random vector $\mathbf{z} = \mathbf{x} + \mathrm{j}\mathbf{y} \in \mathbb{C}^N$ with $\mathbf{x}, \mathbf{y} \in \mathbb{R}^N$ being its real and imaginary part, the PDF $p(\mathbf{z})$ is naturally equivalent to the joint PDF $p(\mathbf{x}, \mathbf{y})$. If $\mathbf{x}$ and $\mathbf{y}$ are zero-mean Gaussian distributed vectors and $[\mathbf{x}^{\mathrm{T}}, \mathbf{y}^{\mathrm{T}}]^{\mathrm{T}}$ is jointly Gaussian, then their joint distribution is completely characterised by the covariance matrix

$$E\left[\begin{bmatrix}\mathbf{x}\\ \mathbf{y}\end{bmatrix}\begin{bmatrix}\mathbf{x}^{\mathrm{T}}\mathbf{y}^{\mathrm{T}}\end{bmatrix}\right] = \begin{bmatrix}E[\mathbf{x}\mathbf{x}^{\mathrm{T}}] & E[\mathbf{x}\mathbf{y}^{\mathrm{T}}]\\ E[\mathbf{y}\mathbf{x}^{\mathrm{T}}] & E[\mathbf{y}\mathbf{y}^{\mathrm{T}}]\end{bmatrix} = \begin{bmatrix}\Sigma_{\mathbf{xx}} & \Sigma_{\mathbf{xy}}\\ \Sigma_{\mathbf{yx}} & \Sigma_{\mathbf{yy}}\end{bmatrix} \in \mathbb{R}^{2N\times 2N}. \tag{3.32}$$

This symmetric matrix has $2N^2 + N$ independent entries which are required to fully specify the covariance of $\mathbf{z}$. To account for all possible covariance information in a complex representation, we need to consider both the covariance matrix $\mathbf{\Sigma_z}$ and the pseudo-

covariance matrix $\mathbf{\Gamma_z}$ which are defined according to

$$\Sigma_{\mathbf{z}} = E[\mathbf{z}\mathbf{z}^{\mathrm{H}}] = \mathbf{\Sigma_{xx}} + \mathbf{\Sigma_{yy}} + \mathrm{j}(\mathbf{\Sigma_{yx}} - \mathbf{\Sigma_{xy}}) \in \mathbb{C}^{N\times N} \tag{3.33}$$

$$\Gamma_{\mathbf{z}} = E[\mathbf{z}\mathbf{z}^{\mathrm{T}}] = \mathbf{\Sigma_{xx}} - \mathbf{\Sigma_{yy}} + \mathrm{j}(\mathbf{\Sigma_{yx}} + \mathbf{\Sigma_{xy}}) \in \mathbb{C}^{N\times N}. \tag{3.34}$$

These two matrices together contain $2N^2 + N$ real independent parameters just like in the real representation. The actual benefit of using one complex vector $\mathbf{z}$ instead of the two real vectors $\mathbf{x}$ and $\mathbf{y}$ to represent a given data set, arise in the special case where the following relations hold

$$\mathbf{\Sigma_{xx}} = \mathbf{\Sigma_{yy}} \tag{3.35}$$

$$\mathbf{\Sigma_{xy}} = -\mathbf{\Sigma_{yx}}. \tag{3.36}$$

A random vector variable $\mathbf{z}$ obeying these properties is called circular-symmetric, which is to say that the PDF satisfies $p(\mathbf{z}) = p(\mathbf{z}e^{\mathrm{j}\phi})$ for any real ϕ [114]. This further implies that the pseudo-covariance matrix $\mathbf{\Gamma_z}$ vanishes, as seen by combining Eqs. (3.34), (3.35) and (3.36). The condition (3.36) implies that the cross-covariance matrices are skew-symmetric according to $\mathbf{\Sigma_{xy}} = -\mathbf{\Sigma_{xy}^{\mathrm{T}}}$, given the identity $\mathbf{\Sigma_{xy}^{\mathrm{T}}} = \mathbf{\Sigma_{yx}}$. For the special case of a scalar circularly-symmetric variable $z = x + \mathrm{j}y$ with $N = 1$, the skew-symmetric property implies that $E[xy] = -E[xy]$ which in turn implies that $E[xy] = 0$ and, hence, that x and y are uncorrelated. A circularly-symmetric complex Gaussian distributed vector variable is denoted $\mathbf{z} \sim \mathcal{CN}(\mathbf{0}, \mathbf{\Sigma_z})$ with the PDF given by [107]

$$p(\mathbf{z}) = \frac{1}{\pi^N \det(\mathbf{\Sigma_z})} \exp\left(-\mathbf{z}^{\mathrm{H}}\mathbf{\Sigma_z}^{-1}\mathbf{z}\right). \tag{3.37}$$

3.4 Modelling of resonant data

The driven response of a resonant system can be accurately modelled by a complex pole series [115] according to

$$S_{21}(\omega) = \sum_k \frac{\alpha_k}{\omega - \omega_k}. \tag{3.38}$$

For measurement frequencies ω close to a particular resonant frequency ω_m, all terms $k \neq m$ in Eq. (3.38) are approximately constant if the resonant frequencies are sufficiently well separated. The response can therefore be approximated as

$$S_{21}(\omega) \approx C + \frac{\alpha_m}{\omega - \omega_m} = \frac{C(\omega - \omega_m) + \alpha_m}{\omega - \omega_m}. \tag{3.39}$$

This is a linear fractional transformation (i.e. a Möbius transformation) in both ω and ω_m, which is equivalent to a Padé approximation of order $1/1$. A Möbius transformation, which can be generally written

$$w = T(z) = \frac{az + b}{cz + 1}, \tag{3.40}$$

where w and z are complex variables and a, b, and c are complex constants, is a conformal mapping that maps generalised circles (i.e. circles or straight lines) onto generalised circles [116]. Hence, if the variable z is taken to be the measurement frequency ω and the poles ω_k and residues α_k are kept constant (thus they determine a, b, and c), we notice that the real axis $\mathrm{Im}\{\omega\} = 0$ is mapped onto a circle in the complex plane. It is well known that such "resonance circles" are observed in the Smith chart when the measurement frequency is swept across a resonance [75]. If we instead keep the measurement frequency constant with $\omega \approx \mathrm{Re}\{\omega_m\}$ and study the S-parameter response due to variations in the resonant frequencies, the result is still a Möbius transformation where the variable z is associated with the resonant frequency ω_m and the constants a, b, and c depend on the measurement frequency ω. The latter situation is illustrated in Fig. 3.1 which shows the distribution of the data $w = T(z)$ given by Eq. (3.40), where z is synthetically generated random data distributed according to

$$\begin{bmatrix} \mathrm{Re}\{z\} \\ \mathrm{Im}\{z\} \end{bmatrix} \sim \mathcal{N}\left(\begin{bmatrix} 0 \\ 0 \end{bmatrix}, \begin{bmatrix} 1 & 0 \\ 0 & P^2 \end{bmatrix} \right) \tag{3.41}$$

with $P^2 = 0.03$. The conformal nature of the mapping T is seen in that the real and imaginary axes in the z-plane are mapped onto circles in the w plane that intersect at right angles at the points $w_0 = T(0) = b$ and $w_\infty = T(\infty) = a/c$. The distribution for w shown in Fig. 3.1 is typical for measured S-parameter data at a fixed frequency near resonance, for a microwave resonator sensor that observes a flowing granular dielectric material, as demonstrated in section 4.2.1 and in Paper III. In this example, z represents the perturbation in the complex resonant frequency ω_m around its mean, which is expected to be normal distributed based on the arguments given in section 3.3.1. In Paper III, we employ maximum-likelihood to estimate the parameters in the model obtained by combining Eqs. (3.40) and (3.41), based on experimental S-parameter data.

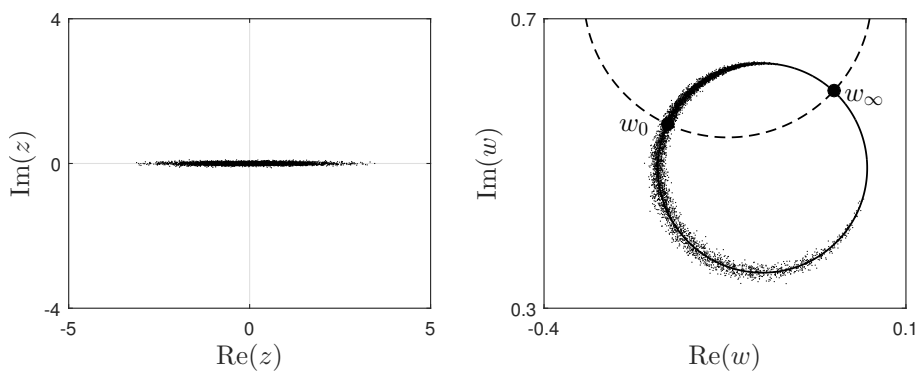

Figure 3.1: Normal distributed complex data z and its mapping through a Möbius transformation $w = T(z)$. Left: realisations of z in the complex plane. Right: data w in the complex plane where each point corresponds to one realisation of z. The points $w_0 = T(0)$ and $w_\infty = T(\infty)$ are indicated by filled circles, and the images of the real and imaginary axis under T are shown by solid and dashed curves, respectively.

Chapter 4

APPLICATIONS, MEASUREMENT TECHNIQUES AND RESULTS

This chapter presents the measurement techniques which have been developed in order to address the two measurement problems considered in the thesis. The industrial applications where these measurement problems are found and the existing alternative measurement techniques are discussed in order to clarify the motivation to our research activities. The main results and conclusions of each individual paper are highlighted, and the papers are finally summarised and compared in a more general perspective.

4.1 Pharmaceutical process monitoring

One challenge in the pharmaceutical industry is to achieve cost-efficient manufacturing of pharmaceutical products under stringent requirements on the product quality, including inter-batch uniformity. The traditional approach in pharmaceutical manufacturing is to maintain a fixed recipe and a fixed set of process control settings once determined based on a comprehensive testing procedure. This is however not adequate to fulfil the increasingly high requirements on the final product quality in the presence of variations in e.g. the raw materials. The pharmaceutical industry is therefore adopting process analytical technologies with the aim to continuously monitor critical process and quality parameters of raw materials and materials under processing. Some of the common pharmaceutical processes are mixing, drying, granulation and spray-coating of solid-state pharmaceutical materials, where the moisture content is a critical process parameter of particular interest to monitor. In this thesis, we consider the spray-coating of particles in Wurster-type fluidised bed processes where the density of particles and the particles' moisture content in different spatial regions inside the vessel is of interest to monitor.

The currently most accurate and reliable methods for moisture content measurements are Karl-Fisher titration [117] and loss-on-drying, but these techniques require

sample withdrawal and can therefore not be used for in-line measurements. Near-infrared (NIR) and Raman spectroscopy are in-line compatible methods which can provide detailed information about the chemical composition of materials, including moisture content [118]. However, due to the short penetration depth at the frequencies employed by these methods, they provide mainly moisture information at the surface of the particles in the direct vicinity of the measurement probe, which may not be representative for the moisture content on a global process scale. Furthermore, these methods are sensitive to deposition of particles or dust on the optical access windows which limits their practical usefulness. Electric capacitance tomography (ECT) is a method where a spatial permittivity distribution is reconstructed from measured capacitances between pairs of electrodes in an electrode array that surrounds the measurement domain, which has been used to monitor fluidised-beds in regions of high particle density [119]. However, the low frequencies employed by ECT (typically in the kHz range) implies that the spatial resolution is dictated by the number of electrodes. Furthermore, the low dielectric losses of pure water at these frequencies makes it difficult for ECT to distinguish moisture content from particle density. Microwave sensing is an attractive measurement modality for fluidised-bed process monitoring due to the possibilities for volume-averaged in-line moisture measurements with high sensitivity. Stray-field microwave resonator sensors have successfully been used for in-line monitoring of fluidised-bed drying and granulation [32, 33]. However, the localised stray-fields limit the sensing region to the vicinity of the sensor head and, thus, this technique cannot be used to perform measurements at arbitrary regions inside the process vessel in a non-intrusive manner.

Our contribution, presented in Paper I, consists of a microwave cavity resonator technique for estimating the complex permittivity in different spatial regions, based on several cavity modes in the metal process vessel. This technique allows us to gather information about moisture and particle density from different spatial regions inside the vessel in a non-invasive manner, where small amounts of moisture can be detected due to the high sensitivity of the high-Q resonant cavity modes.

4.1.1 Microwave cavity measurement system

The fluidised-bed process vessel that we consider here is normally used for particle coating and drying processes in laboratory-scale at AstraZeneca R&D in Mölndal, Sweden. The vessel is shown in Fig. 4.1, which also shows the two coupling loops that we use to excite the cavity modes inside the vessel and measure their resonant frequencies. The vessel is originally equipped with a number of dielectrically sealed openings in the metal wall to allow for visual inspection and access by other measurement probes. We cover these holes (in particular the two inspection windows) externally by metal foil to mitigate the radiation losses of the cavity modes. A perforated metal plate is also placed at the top of the vessel where the fluidising air exits, to prevent electromagnetic radiation losses and to create an interior cavity volume that is feasible to model accurately. With these measures, we obtain unloaded Q-values in the range from 3 000-10 000 for the lowest modes in the empty cavity. Figure 4.2 shows the electric field of the eight resonant modes that we can reliably identify based on the resonant frequencies without risk

of confusion, where the fields are computed using a finite-element model implemented in Comsol Multiphysics [120]. Figure 4.3 shows the S-parameters measured with a commercial VNA (Agilent E8361A). This instrument is controlled by a PC via GPIB interface to perform repeated frequency sweeps (one sweep with 2 seconds duration is repeated every 10 seconds) throughout the duration of a process experiment, where the repetition speed is mainly limited by the data transfer. From the transmission coefficient S_{21}, we estimate the complex resonant frequency associated with each mode using subspace-based system identification [98]. The resulting pole-series model $\hat{S}_{21}$ as expressed in Eq. (2.28) is shown in Fig. 4.3 together with the real part of the estimated resonant frequencies. The modes TE_{111}-TE_{114} each forms a degenerated mode-pair in a perfectly axi-symmetric cavity. However, in the process vessel, the resonant frequencies of each such mode-pair are separated due to the foil-covered inspection windows that resemble a local outward displacement of the metal boundary. The high-frequency mode of each pair has maximum electric field at the azimuth locations of the windows, as explained by Eq. (2.26). These modes are found to be more stable than the low-frequency associates, which have strong surface currents flowing across the junction between the cavity wall and the foil. Therefore, we use only the high-frequency polarisation in each of these mode-pairs for the permittivity estimation.

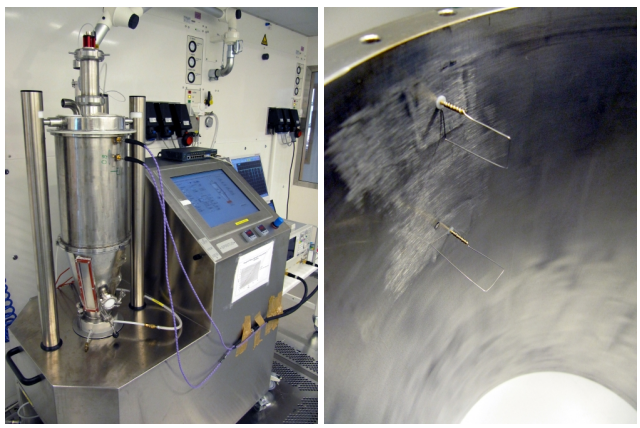

(a) (b)

Figure 4.1: (a) The fluidised-bed process vessel connected to a network analyser and a process control unit, and (b) the coupling loops.

Temperature variations is an inescapable aspect of fluidised-bed processing, due to the inflow of warm fluidising air at the bottom of the vessel and the cooling caused by evaporation of solvents during spray-coating. Temperature variations have a significant impact on the resonant frequencies as it leads to non-uniform thermal expansion of the vessel walls with long time-constants, as shown in Fig. 4.4. The resonant frequency perturbations due to temperature variations is comparable in size to the perturbations resulting from the permittivity variations we intend to measure, which is illustrated in Fig. 4.5. Our strategy to circumvent this issue is to parametrise jointly the perturba-

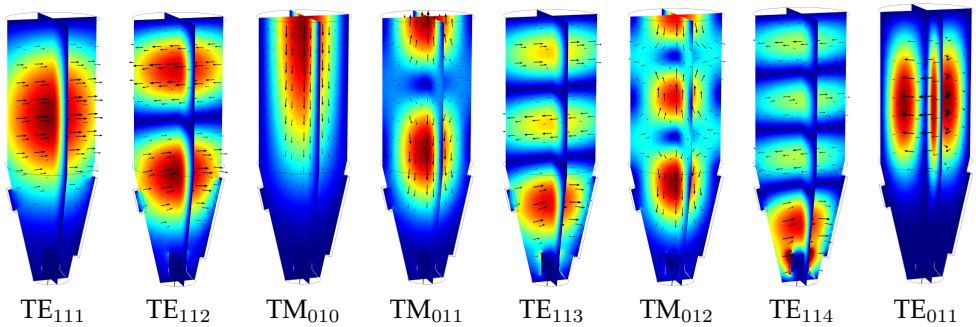

Figure 4.2: Electric field of the resonant cavity modes in the process vessel that are used to sense the spatial permittivity distribution.

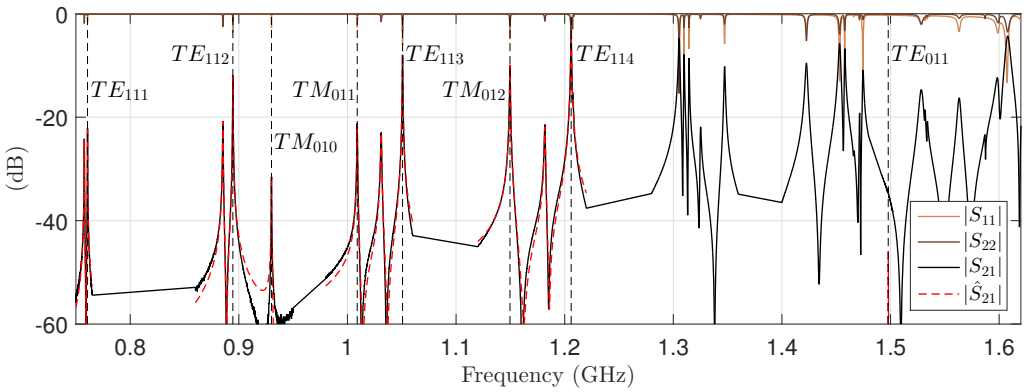

Figure 4.3: Measured S-parameters of the empty process vessel using a segmented frequency sweep, and the estimated pole-series model $\hat{S}_{21}$. The dashed vertical lines show the real part of the estimated resonant frequencies.

tions in the permittivity distribution and the shape of the cavity walls using the spatial basis functions illustrated in Fig. 4.6. We estimate the permittivity and shape parameters based on the measured resonant frequency perturbations as well as temperature measurements at several locations on the vessel wall. The temperature measurements serve to "assist" in the estimation of the shape parameters, so that the microwave response can be used mainly to determine the permittivity parameters based on an overdetermined system of equations. The sensitivities in the resonant frequencies with respect to material and shape perturbations are calculated from the finite-element model using Eqs. (2.25) and (2.26). For further details on the estimation procedure, the reader is referred to Paper I.

The estimated complex permittivity in each subregion as function of process time is presented in Paper I for three different process experiments: (i) film-coating of microcrystalline cellulose (MCC) particles by Mannitol and a binding polymer at a low spraying rate that yields stable process conditions, (ii) film coating by the same sub-

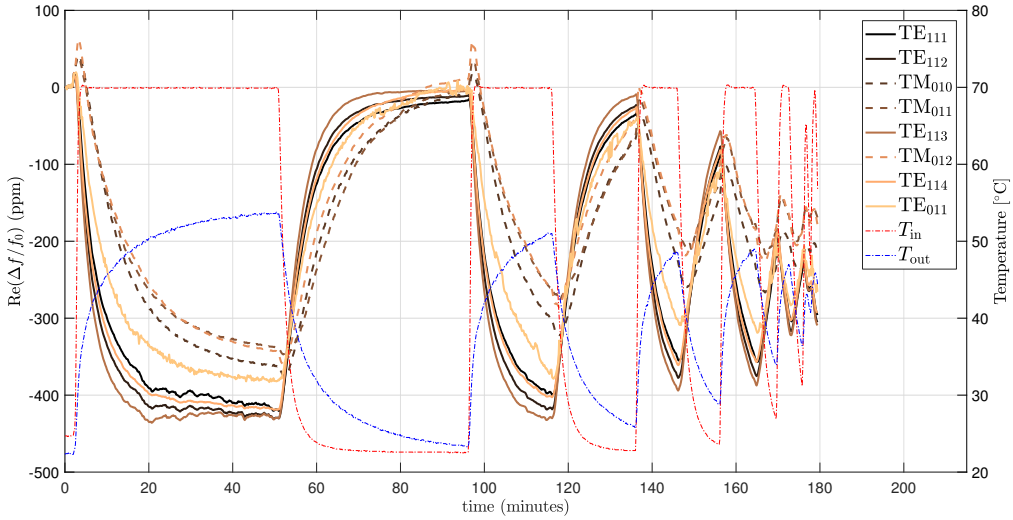

Figure 4.4: Relative shift in the resonant frequencies in parts-per-million (ppm) for the empty vessel during cyclic heating and cooling. The dash-dotted curves show the temperature of the fluidising air at the inlet and outlet of the vessel, respectively.

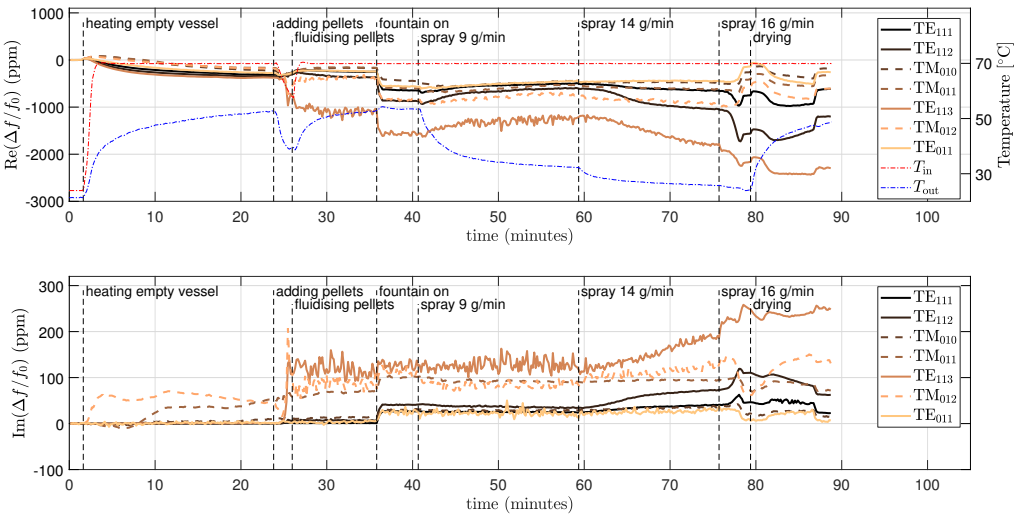

Figure 4.5: Real and imaginary part of the resonant frequency shift during spray-coating of MCC pellets by Mannitol and a binding polymer dissolved in water. The spraying rate is increased successively which eventually leads to partial agglomeration with particles adhering to the vessel walls. The dashed vertical lines and the associated labels indicate external changes in the process settings.

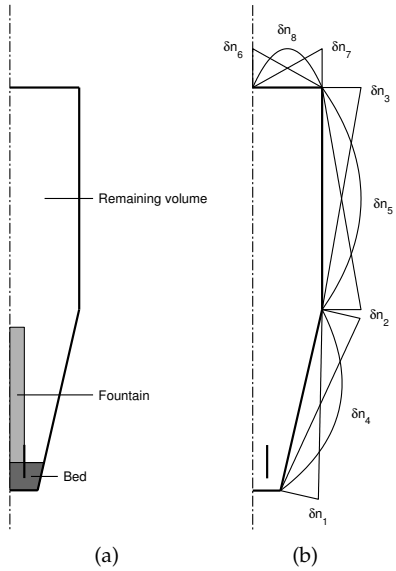

Figure 4.6: Parametrisation of (a) the permittivity in three distinct subregions and (b) perturbations in the shape of the cavity walls.

stance at high spraying rate that leads to agglomeration and process collapse (see also Fig. 4.5), and (iii) MCC particles sprayed with a high-loss saline solution at increasingly high spraying rates leading to agglomeration. We conclude that several aspects of the process state is reflected in the estimated permittivities, such as (i) the material re-distribution when the particle fountain is turned on, (ii) the growth in particle size during coating, and (iii) material build-up on the cavity walls during agglomeration. Furthermore, by analysing the covariance between the estimated permittivity's real and imaginary part, it is possible to detect changes in dielectric losses resulting from the spray liquid, which is highly interesting from the application point of view. One possibility for improving this measurement technique is therefore to increase the measurement speed significantly, to enable more reliable covariance estimates from larger data samples with a higher temporal resolution.

4.2 Detection of objects in granular flows

As stated in the section 1.1, the detection of undesirable objects is an important issue in many material processing industries. Metal detectors and X-ray systems are dominating the market for inspection systems to detect solid contaminants in bulk materials and packaged product items, but these methods have limited detection capabilities for low-density dielectric contaminants such as plastics, wood and rubber [121]. Several alternative measurement methods have therefore been investigated for undesirable object detection, including acoustic and ultrasonic measurements [122–124], thermal imaging [125] and terahertz-wave measurements [126]. Although these methods show a varying degree of success for certain combinations of objects and background materials, using different modes of material transportation, it can be concluded that no method is alone capable of detecting all occurring objects independently of the background material.

At present, metal detectors is the only industrially feasible method to detect objects in granular materials that flow by the aid of gravity, because X-ray imaging is hindered by the irregular movement of the flowing particles [127]. Since metal detectors lack sensitivity to dielectric media, it is currently an unresolved problem to detect dielectric objects in flowing granular materials in an industrially viable manner. This is the motivation to the research presented in this thesis, where we aim to develop an industrially feasible microwave measurement technique for detecting dielectric objects of different composition with smallest possible size in flowing powders and granulates.

4.2.1 Microwave detection systems

This section summarises the work contained in Papers II-V on the topic of object detection in powders, including the detection system developments, results and conclusions.

Short cavity sensor and simulation-based detection evaluation

In paper II, the first step to approach the current detection problem was to develop a microwave sensor for highly sensitive permittivity measurements inside metal pipes. A sensor concept based on a resonant cavity operating below the cut-off frequency of a 1.5 inch metal pipe was selected for this purpose, where a dielectric pipe with the same inner diameter as the metal pipe is used to guide the material under test (MUT) through the cavity. The cavity's total volume was intentionally kept small to increase the sensitivity to an object of given size. The geometry of the cavity, including its coupling loops and the dielectric material, were optimised by means of FEM-simulations. Here, the objective was to maximise the number of clearly identifiable modes in the frequency range 2-3 GHz, which is the supported frequency range of a high-speed microwave measurement instrument that is available within the scope of the project. The electric field of the five available sensing modes and the S-parameters of the sensor prototype are shown in Figures 4.7 and 4.8. The sensing modes, except TE_{111}, have a relatively uniform electric field over the cross-section of the pipe which is beneficial for the ability to detect an object irrespectively of its transverse position. In Paper II, we investigate

the detection performance for a power detector on the form of Eq. (3.22), based on computed eigenfrequencies given a stochastic permittivity that represents the background material together with a dielectric object. The random permittivity $\epsilon(\vec{r}) \sim \mathcal{N}(\mu, \sigma^2)$ is generated on a 3D spatial grid to have the autocorrelation

$$\mathrm{cov}\left(\epsilon(\vec{r}), \epsilon(\vec{r}+\Delta\vec{r})\right) = \sigma^2 \exp\left(-\frac{|\Delta\vec{r}|^2}{2\xi^2}\right), \tag{4.1}$$

where ξ is a correlation length. Based on these computational studies, we conclude that the detection performance is improved by an increasing number of modes used in the detector, and that the correlation length ξ in relation to the size of the object and the sensor plays an important role for the detection performance.

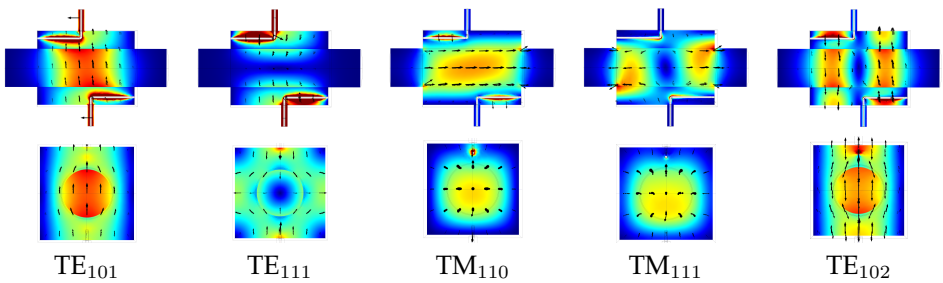

Figure 4.7: Electric field of the resonant modes between 2-3 GHz for the short sensor.

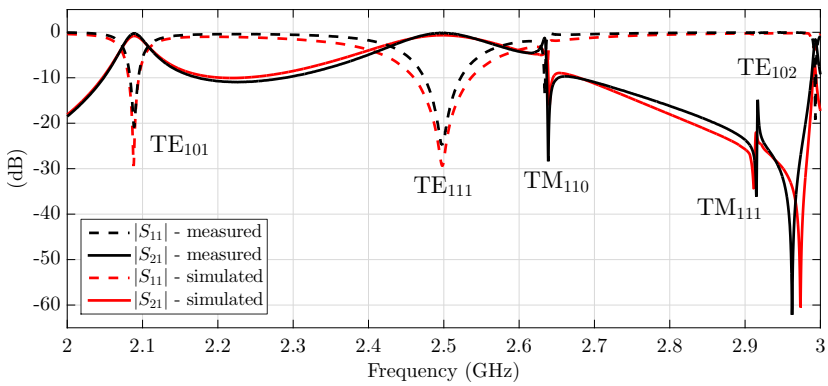

Figure 4.8: Measured and simulated S-parameters of the short sensor.

Experimental detection evaluation using a Möbius transformation signal model

In Paper III we proceed to study the detection performance experimentally. Here, we use a custom-design measurement electronics that provides the high measurement speed required for the current application where at least a few hundred measurements per

second is required for an object passage to be temporally well-resolved. This electronics (described in more detail in Paper III) resembles a VNA but provides measurement data that is uncalibrated with respect to the true S-parameters. The calibration aspect, together with a relatively poor frequency resolution of 5 MHz, implies that the data from this instrument cannot be used to estimate the complex resonant frequencies of the sensor in an absolute sense in a reliable manner. Therefore, we use the uncalibrated S-parameter data at single measurement frequencies close to resonance for each mode, as the input to a detection algorithm after a particular pre-processing procedure has been applied. If we denote the raw uncalibrated measurement data by w (which resembles S_{21}), this pre-processing relies on the model

$$w_m[n] = T_m(z_m[n]) = \frac{a_m z_m[n] + b_m}{c_m z_m[n] + 1} \tag{4.2}$$

where the complex variable z_m is distributed according to Eq. (3.41). We emphasize that w_m, measured at a frequency ω where the resonant mode m is excited, varies stochastically with respect to time due to the permittivity fluctuations of the flowing material. The parameters, a_m, b_m, c_m, and P_m, which apply at the frequency ω, are estimated by maximum-likelihood from the data samples $\{w_m[n]\}_{n=0}^{N-1}$ using iterative maximisation of the non-linear log-likelihood function. Given the estimates of a_m, b_m, c_m, we use the inverse of the mapping T_m in Eq. (4.2) to obtain the data z_m which, to a good approximation, is Gaussian distributed and hence facilitates the derivation of an LRT detector.

Based on the arguments in Section 3.4, we may interpret the mapped data as being linearly related to the perturbation $\Delta\omega_m$ in the complex resonant frequency of mode m around its mean, according to $z_m = \zeta\Delta\omega_m$. Here, ζ is a complex constant such that, for sufficiently small losses, the direction of $\Delta\omega_m$ in the complex plane that corresponds to increasing material density is mapped onto the real part of z_m, which has unit variance. The relation between the background material's inclusion permittivity and volume fraction on the effective permittivity, the complex resonant frequencies, the S-parameters and the mapped variable z is illustrated in Fig. 4.9 by Monte-Carlo simulation. Here, it is clearly seen how an object with lower losses than the background yields an increase in $\mathrm{Im}(z)$. Figure 12 in Paper III presents similar results based on measurement data.

In Paper III, we conclude that the data model presented above is appropriate for modelling the statistics of the measurement response and the systematic errors associated with the uncalibrated instrument. An instantaneous power detector applied to the mapped Gaussian data is used to evaluate the detection performance based on measurements on low-loss polyethylene powder and test objects consisting of wood, polyvinylchloride and polyethylene. It is concluded that this approach is efficient for detecting objects that have significant contrast in the dielectric losses as compared to the background material.

Matched filter detector for the short cavity sensor

In Paper IV, we employ a signal processing algorithm that aims to exploit the temporal variation in the data to improve the detection in situations where the object is difficult to detect based solely on the locus of the S-parameters in the complex plane. This typically occurs when the object has similar loss tangent as the background material. We

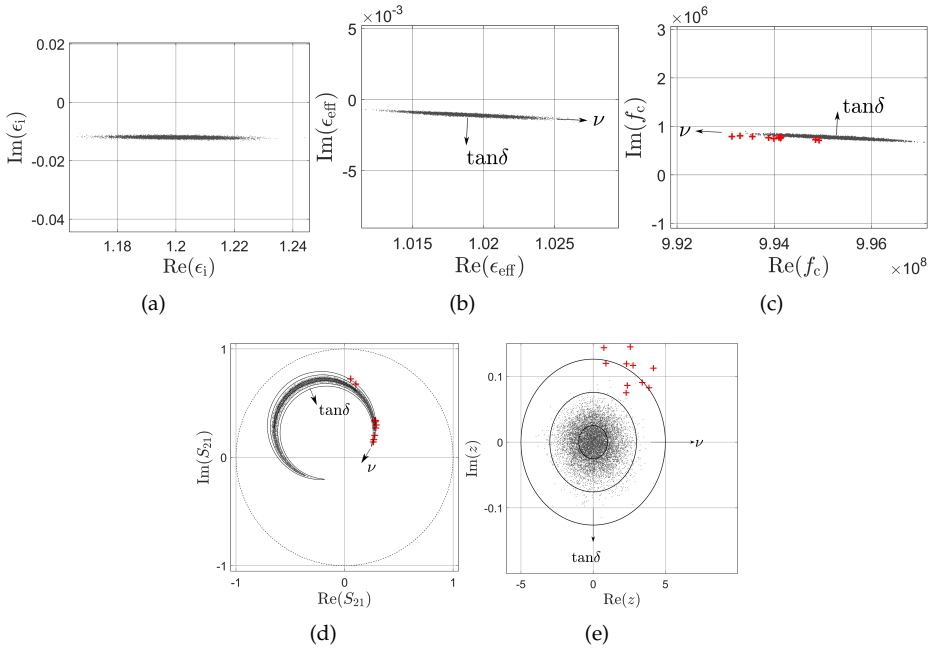

Figure 4.9: Simulation-based illustration of a stochastic dielectric mixture and the resulting resonant data. (a) Realisations of the inclusion permittivity ϵ_{i} with average loss tangent $\tan\delta = 0.01$, (b) Maxwell-Garnett effective permittivity ϵ_{eff} given the stochastic volume fraction $\nu \sim \mathcal{N}(0.1, 0.01^2)$, (c) complex resonant frequencies f_{c} for a cavity with $Q = 1000$ where ϵ_{eff} occupies the entire cavity volume, (d) S_{21} given Eq. (3.39) with $C = 0.1 - 0.1\mathrm{j}$, $\alpha_m = 7 \cdot 10^5$ and $\omega = 2\pi\mathrm{Re}(E[f_c])(1 + 0.1/Q)$, and (e) mapped data z. The red crosses show the effect of adding a lossless object with permittivity $\epsilon_{\mathrm{r,obj}} = 2.4$ that occupies 0.2% of the cavity volume. The arrows in (b)-(e) indicate the directions of increasing volume fraction ν and loss tangent $\tan\delta$. The solid curves in (d)-(e) are contour lines of the estimated PDF at 1, 3, and 5 standard deviations.

formulate a noise-whitening matched filter detector that incorporates the temporal and inter-channel correlation of the noise due to the background material, and pre-recorded target waveforms obtained from measurements on single object passages. Based on detection experiments using the same experimental setup as in Paper III, we conclude that the matched filter detector yields no significant detection improvement as compared to the previously studied power detector. Our interpretation of this result is that, for the current sensor, the temporal waveforms due to an object passage are similar to the temporal waveforms due to the background material and, hence, that no improvement is gained by incorporating temporal information in the detector.

Long cavity sensor and temporal signals analysis

The variation in the measurement data that is caused by the permittivity variations of a flowing powder stems mainly from fluctuations in the local powder density. To some extent, these fluctuations propagate downstream with the flow velocity, but the maximum cross-correlation between the density at a certain point and at another point further downstream, decays with the separation distance due to mixing effects. The idea pursued in Paper V is therefore to use a longer sensor that measures over a sufficiently long flow distance, so that the correlation of the material density (and hence the permittivity) at the two ends of the sensor has decayed substantially. A longer sensor can also support a yet larger number of resonant modes in the frequency interval 2-3 GHz, where some of these modes feature a high order field variation in the direction of the flow. The S-parameters of the prototype sensor device is shown in Fig. 4.11 and the electric field of the resonant modes of interest is shown in Fig. 4.10. For a high-order mode such as TE_{109}, the mixing of the powder that occurs inside the sensor tend to have a smoothing effect on the temporal waveforms (such as S_{21} measured over time). On the contrary, a small dielectric object that travels downstream with a certain velocity yields a temporal waveform that resembles the spatial sensitivity of that mode along the cylinder axis. We expect that this temporal diversity can be exploited to improve the detection by a matched filter detector on the form of Eq. (3.20), and this hypothesis is investigated in Paper V.

The pre-processing of the S-parameter data employed in this paper is based on linear operations, in contrast to the maximum-likelihood estimation used in Papers III-IV, which makes the current signal processing algorithm straight-forward to implement in a real-time detection system. For details on the detection algorithm and the associated pre-processing and noise statistics estimation, the reader is referred to Paper V.

We evaluate the detection performance using a new experimental setup (illustrated in Fig. 4.12) that allows for automatised release of a large number of test objects, which makes it possible to quantify the detection performance more accurately and, hence, to draw more detailed conclusions. Table 4.1 presents the AUC for the detection of sperical steel and Delrin objects of varying diameter in flowing MCC granules and glass beads. Based on these results, it can be concluded that the matched filter detector performs significantly better than both the temporal power detector and the spatial power detector employed in Paper III, for all combinations of object and powder.

In order to compare the performance of the long and short sensor, all experiments

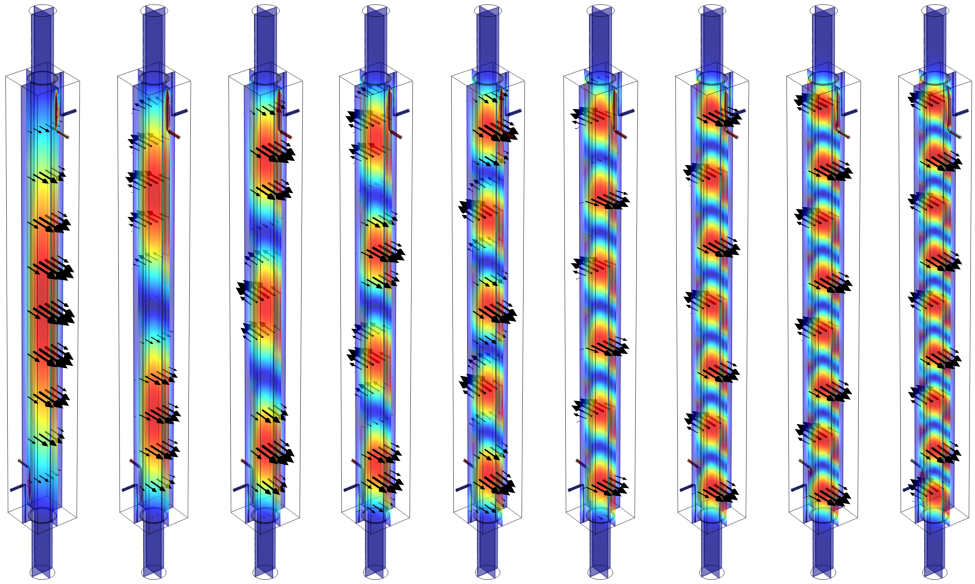

Figure 4.10: Electric field of the nine lowest resonant modes TE_{101}-TE_{109} in the long sensor.

that lead to the results in Tab. 4.1 are simultaneously performed with the short sensor mounted directly upstream of the long sensor, so that both sensors observe the same background material and the same objects. This experimental arrangement is shown in Fig. 4.12. By applying the signal processing algorithm i Paper V also to the data from the short sensor, we obtain the AUC-values presented in Tab 4.2. For the short sensor, we notice that the spatial power detector performs uniformly better than the matched filter. This agrees with the results in Paper IV, and supports our hypothesis that a sufficiently long flow distance is required to obtain sufficient mixing for the temporal detectors to be more effective than an instantaneous power detector. Furthermore, by comparing the results in Tables 4.1 and 4.2, we notice that the spatial power detector in the short sensor performs better than the matched filter detector in the long sensor, presumably due to the short sensor's higher sensitivity to an object of given size. A possible future option that combines the positive aspects of each design, is therefore to use multiple short sensors mounted in series with an appropriate separation distance, and process the data from the entire sensor array jointly in a matched filter detector.

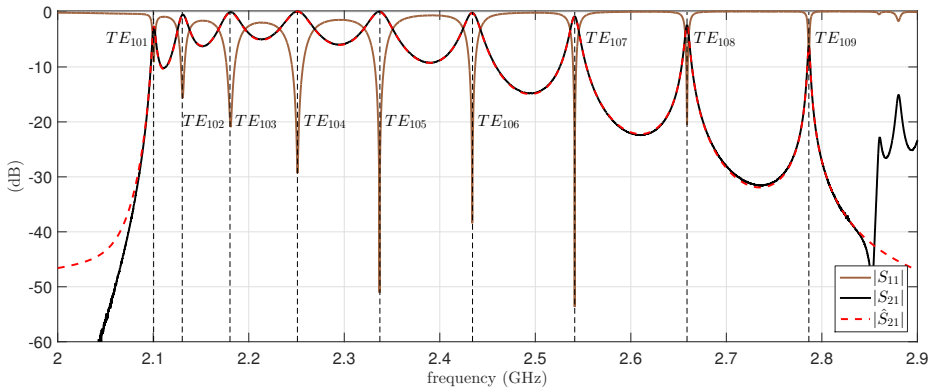

Figure 4.11: Measured S-parameters of the long sensor and the estimated pole-series model $\hat{S}_{21}$. The dashed vertical lines show the real part of the estimated resonant frequencies.

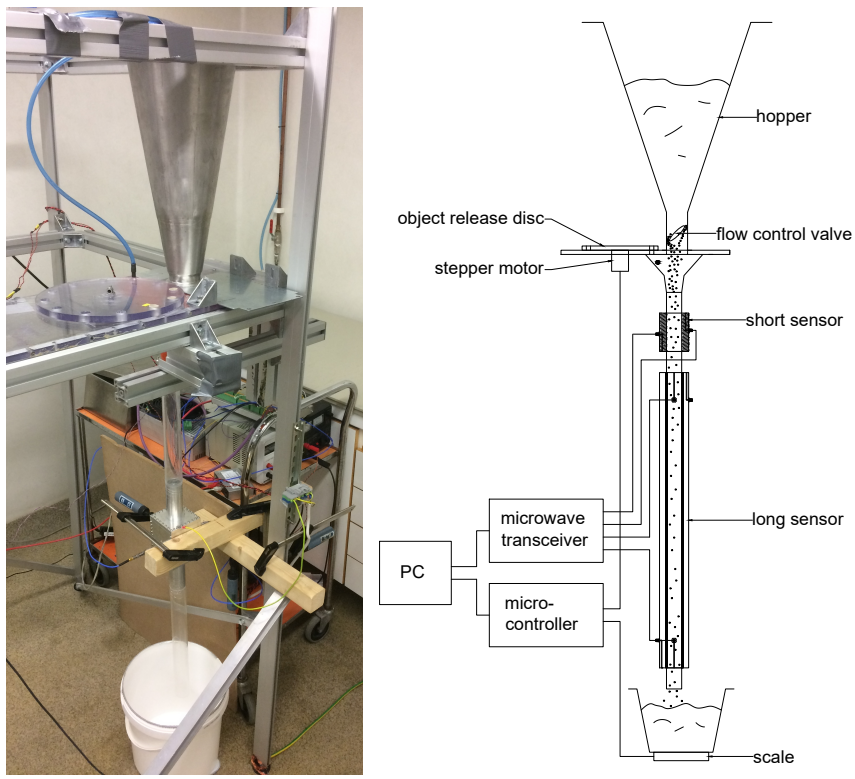

(a) (b)

Figure 4.12: Experimental setup for studying the detection of objects in flowing granular materials. (a) photo including the short sensor, (b) schematic drawing with the short and long sensor mounted in series.

Table 4.1: Long sensor: Area under the ROC curve for the detection of spherical test objects in flowing MCC pellets and glass beads, using the spatial power detector (SPD), temporal power detector (TPD) and matched filter detector (MF), as described in Paper V.

	MCC pellets (100 kg/h)			glass beads (100 kg/h)		
	SPD	TPD	MF	SPD	TPD	MF
steel 4mm	0.998	1.000	1.000	1.000	1.000	1.000
steel 2mm	0.570	0.520	0.576	0.744	0.830	0.984
delrin 8mm	1.000	1.000	1.000	1.000	1.000	1.000
delrin 6mm	1.000	1.000	1.000	1.000	1.000	1.000
delrin 4mm	0.788	0.603	0.865	0.994	0.993	1.000
delrin 2mm	0.516	0.519	0.560	0.553	0.552	0.626
pepper 4mm	0.873	0.873	0.965	1.000	1.000	1.000

Table 4.2: Short sensor: Area under the ROC curve for the detection of spherical test objects in flowing MCC pellets and glass beads, using the spatial power detector (SPD), temporal power detector (TPD) and matched filter detector (MF).

	MCC pellets (100 kg/h)			glass beads (100 kg/h)		
	SPD	TPD	MF	SPD	TPD	MF
steel 4mm	1.000	1.000	0.999	1.000	1.000	1.000
steel 2mm	0.524	0.542	0.522	0.987	0.974	0.951
delrin 8mm	1.000	1.000	1.000	1.000	1.000	1.000
delrin 6mm	1.000	1.000	1.000	1.000	1.000	1.000
delrin 4mm	0.966	0.932	0.940	1.000	0.998	1.000
delrin 2mm	0.520	0.538	0.533	0.635	0.632	0.598
pepper 4mm	0.986	0.942	0.959	1.000	1.000	1.000

4.3 Estimation and detection based on resonant sensor data

This section aims to compare the measurement techniques presented in Paper I-V in the sense of identifying commonalities in the steps where data is acquired, processed and finally used to infer the desired measurement information. Figure 4.13 gives an illustrative summary of the steps that constitute the measurement technique presented in each paper. Since all measurement techniques are based on cavity resonators featuring several resonances that observe a fluctuating permittivity distribution, we imagine a common model for the "true" S-parameter response which is observed using a measurement instrument with certain characteristics.

In Paper I, we use a commercial VNA instrument that provides highly accurate and well-calibrated S-parameter measurements at high frequency resolution but at relatively low sampling speed. From this high-quality S-parameter data on a dense frequency grid, we estimate the corresponding complex resonant frequencies ω_m using subspace-based system identification. On the contrary, in Paper III-V, we use a custom electronics (described in more detail in these papers) that provides high measurement speed but low frequency resolution and, in addition, the data is uncalibrated and hence associated with systematic errors. It is therefore inappropriate to perform a direct estimation of the complex resonant frequencies based on the data from this instrument. Instead, we aim to map the S-parameter data at individual frequencies onto a new set of data, here represented by the complex variable z, that resembles the variation of the complex resonant frequencies around their mean values, and therefore tend to be Gaussian distributed. Depending on the variability of the underlying resonant frequencies in relation to the associated resonator bandwidth $B_m = \mathrm{Re}\{\omega_m\}/Q_m$, the data distribution turns out differently where a big variability yields highly curved arc-shaped regions and small variability yields rather Gaussian-shaped clouds. For curved clouds, we use a mapping that involves maximum-likelihood estimation of parameters in a Möbius transformation (Paper III-IV), whereas for clouds that are nearly Gaussian-shaped, the mapping consist merely of linear high-pass filtering and de-correlation of the real and imaginary parts (Paper V). It should be emphasised that while mapping uncalibrated S-parameter data to Gaussian data that is normalised in some generic manner, we lose the ability to estimate the permittivity of the material mixture in the absolute sense. However, sensitive detection is still possible based on the dielectric contrast between an object and the background material. Expressed differently, the complex Gaussian data z obtained from uncalibrated measurements at a single frequency is related to the complex resonant frequency perturbation via an unknown complex constant ζ according to $z = \zeta\Delta\omega_m$. Here, ζ involves the loss tangent of the effective permittivity together with other unknown effects in the uncalibrated measurement.

The final step is the inference of the desired measurement information based on the data that resembles the resonant frequencies. In Paper I, the desired output is a spatial permittivity profile that we estimate by solving a linearised inverse problem by means of a regularised least squares procedure. In Paper II-V the output is a detection decision obtained by a detection algorithm whose degree of correctness may be illustrated by an ROC curve.

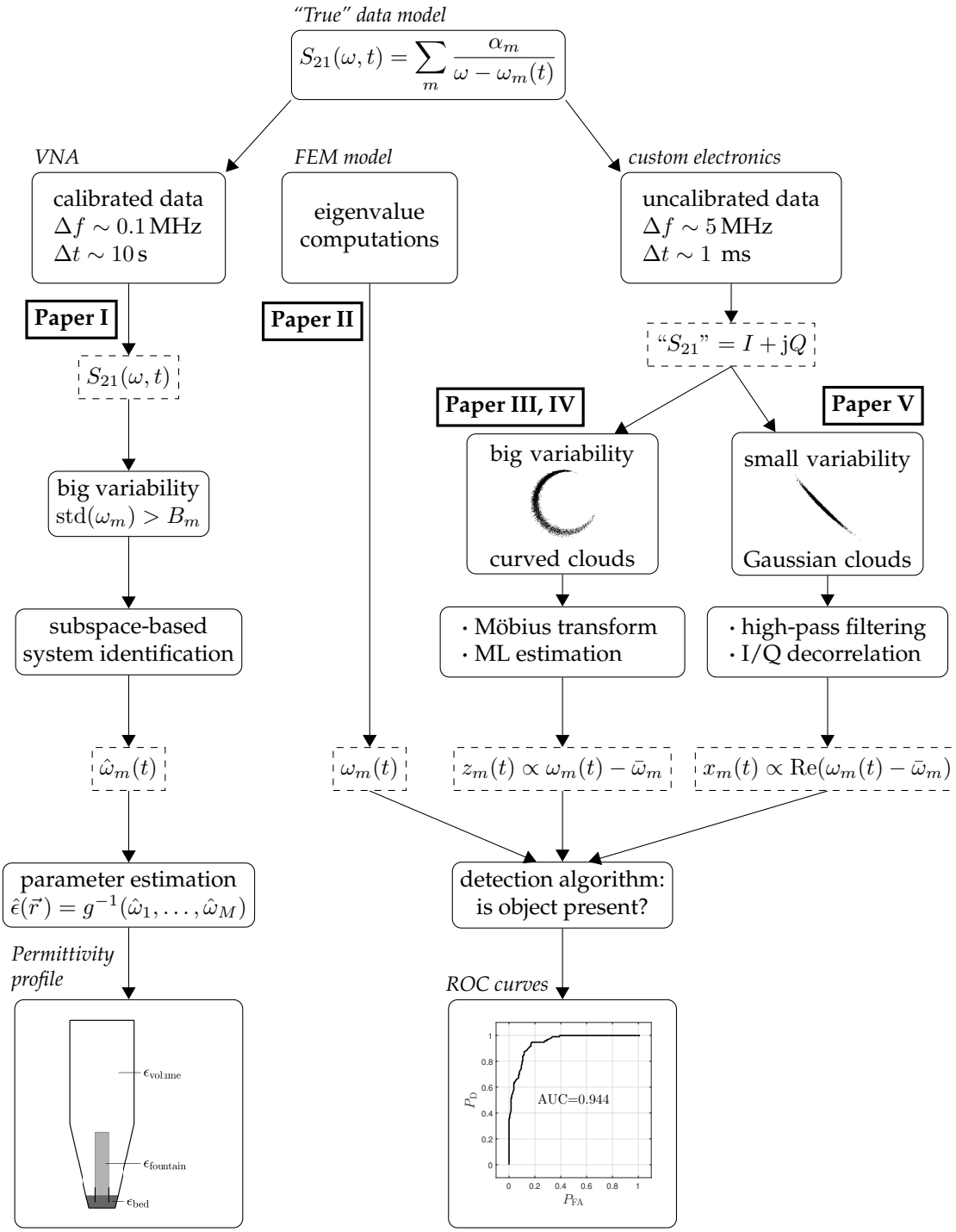

Figure 4.13: Illustrative summary of the data acquisition and analysis in Paper I-V.

Chapter 5

Conclusion

This thesis presents microwave measurement techniques for use in the process industry, where we consider the electromagnetic design and modelling of the sensors, the development of signal processing algorithms, and the experimental evaluation in relevant process-industrial scenarios. The measurement techniques are based on resonant cavities to enable highly sensitive measurements of the permittivity variations inside closed metal vessels or metal pipes.

Two industrial measurement problems are studied in detail, where the first is to monitor the internal state of a pharmaceutical fluidised-bed processes. This is done by viewing the metal vessel that contains the process as a cavity resonator. Based on scattering parameters measured with a vector network analyser, we estimate the complex resonant frequencies of eight different cavity modes. From the resonant frequencies, we estimate the parameters in a low-order model for the spatial permittivity distribution, where the sensitivities to material and shape perturbations are computed from cavity perturbation formulas using a detailed finite-element model. We conclude that several aspects of the process state can be observed based on the estimated permittivity, including the growth in particle size, the presence of lossy spraying liquids and the onset of agglomeration, although no process quality attributes are estimated in the absolute sense. It is expected that the estimation of statistical quantities, such as the covariation between the real and imaginary permittivity, can be significantly improved by a considerable increase in the measurement speed. Thereby, more accurate information about the material losses and hence the liquid content of the particles may be derived.

The second problem is to detect undesirable objects in granular dielectric materials flowing through a pipe. Two cavity resonator sensors with different lengths in the flow direction have been developed for this purpose. The measurements are performed using a high-speed microwave instrument that provides data with considerable systematic errors with respect to the true scattering parameters. Different pre-processing algorithms are therefore investigated which utilise the stochastic variation of the flowing background material to remove the effects of the uncalibrated instrument. The pre-processed data is subsequently used in detection algorithms derived from the likelihood-ratio test,

which take the form of power detectors or matched filters depending on the assumptions. We conclude that a significant gain in detection performance can be achieved by using a matched filter detector if the sensor extends over a sufficiently long flow distance.

This thesis demonstrates the usefulness of resonant microwave sensors that exploit multiple resonant modes with diverse spatial field distributions to improve the measurement performance and to address new measurement problems. Furthermore, it is demonstrated that model-based signal processing algorithms that incorporate knowledge about the underlying physics can lead to distinct improvements in the estimation and detection performance for process-industrial measurement problems. These improvements become particularly clear in more challenging measurement situations that involve larger variations in the permittivity and in the resulting measurement data. The model-based approach to electromagnetic measurements is further aided by the advancement of numerical simulation tools and the rapid increase in available computing power, which makes it feasible to address increasingly complex measurement problems.

Acknowledgments

This thesis implies the end of five very rewarding and joyful years as a doctoral student, where I have had the privilege to work with many friendly and skilled people on problems that I find both scientifically interesting and industrially useful. I would therefore like to take the opportunity to express my gratitude to a number of people.

First and foremost, my sincere thank goes to Thomas Rylander, for giving me the opportunities as an undergraduate student that eventually led me into this exiting trajectory. I hope that I have managed to pick up as much as possible of your admirable thoughtfulness, patience, language and thorough approach to learning and understanding. My sincere appreciation goes also to Tomas McKelvey, for sharing your vast knowledge and for hosting such a pleasant and stimulating research group. To Joakim Nilsson, Sven-Gunnar Bodell, Stig Norén and Mikael Reimers at Food Radar, thank you for welcoming me into your company, for the great pleasure of working with you and for helping me with all sorts of problems at any time with your inexhaustible energy. To Lubomir Gradinarsky, Staffan Folestad and Anders Holmgren, thank you for the nice and interesting time at AstraZeneca.

To current and former colleagues in the signal processing group and at the department, in particular to Johan Winges, Livia Cerullo, and Oscar Talcoth for being such good role models and for the nice times. To Johan, Jonathan, Nina, Linnéa and Lars for the immensely nice coffee and lunch breaks. Lars, your spirit remains. Thanks to Olov and Klas for all the nice lunches.

Not least, many thanks go to my family for your support and encouragement. To mum, for your industriousness, to dad for your curiosity, and to Anna and Per for making me try to keep up with you.

Finally, thank you Hanna for the best company through life that anyone could ask for, and to Alma for a greater happiness than I knew existed.

Johan Nohlert
Göteborg, February 2018

BIBLIOGRAPHY

[1] D. C. Hinz, "Process analytical technologies in the pharmaceutical industry: the FDA's PAT initiative," *Analytical and Bioanalytical Chemistry*, vol. 384, pp. 1036–1042, 2006.

[2] J. C. Maxwell, "A dynamical theory of the electromagnetic field," *Philosophical Transactions of the Royal Society of London*, vol. 155, pp. 459–512, 1865.

[3] J. D. Jackson, *Classical Electrodynamics*. John Wiley & Sons, 3 ed., 1999.

[4] A. von Hippel, *Dielectrics and Waves*. John Wiley & Sons, 1954.

[5] A. Sihvola, *Electromagnetic Mixing Formulas and Applications*. The Institution of Engineering and Technology, 1999.

[6] J. C. Maxwell Garnett, "Colours in metal glasses, in metallic films, and in metallic solutions. II," *Philosophical Transactions of the Royal Society of London*, vol. 205, pp. 237–288, 1906.

[7] G. Kristensson, S. Rikte, and A. Sihvola, "Mixing formulas in the time domain," *Journal of the Optical Society of America A*, vol. 15, no. 5, pp. 1411–1422, 1998.

[8] A. Kraszewski, "Microwave aquametry: An effective tool for nondestructive moisture sensing," *Subsurface Sensing Technologies and Applications*, vol. 2, no. 4, pp. 347–362, 2001.

[9] W. Meyer and W. Schilz, "A microwave method for density independent determination of the moisture content of solids," *Journal of Physics D: Applied Physics*, vol. 13, no. 10, pp. 1823–1830, 1980.

[10] L. Gradinarsky, H. Brage, B. Lagerholm, I. Niklasson Björn, and S. Folestad, "In situ monitoring and control of moisture content in pharmaceutical powder processes using an open-ended coaxial probe," *Meas. Sci. Technol.*, vol. 17, no. 7, pp. 1847–1853, 2006.

[11] B. L. Shrestha, H. C. Wood, and S. Sokhansanj, "Prediction of moisture content of alfalfa using density-independent functions of microwave dielectric properties," *Meas. Sci. Technol.*, vol. 16, no. 5, pp. 1179–1185, 2005.

[12] A. W. Kraszewski, S. Trabelsi, and S. O. Nelson, "Comparison of density-independent expressions for moisture content determination in wheat at microwave frequencies," *Journal of Agricultural Engineering Research*, vol. 71, no. 3, pp. 227–237, 1998.

[13] S. Trabelsi and S. O. Nelson, "Density-independent functions for on-line microwave moisture meters: a general discussion," *Meas. Sci. Technol.*, vol. 9, no. 4, pp. 570–578, 1998.

[14] D. A. G. Bruggeman, "Berechnung verschiedener physikalischer konstanten von heterogenen substanzen: I. Dielektrizitätskonstanten und leitfähigkeiten der mischkörper aus isotropen substanzen," *Annalen der Physik*, vol. 5, no. 24, pp. 636–664, 1935.

[15] R. J. Elliott, J. A. Krumhansl, and P. L. Leath, "The theory and properties of randomly disordered crystals and related physical systems," *Rev. Mod. Phys.*, vol. 46, no. 3, pp. 465–543, 1974.

[16] A. Sihvola, "Self-consistency aspects of dielectric mixing theories," *IEEE Trans. Geosci. Remote Sens.*, vol. 27, no. 4, pp. 403–415, 1989.

[17] O. Pekonen, K. Kärkkäinen, A. Sihvola, and K. Nikoskinen, "Numerical testing of dielectric mixing rules by FDTD method," *Journal of Electromagnetic Waves and Applications*, vol. 13, no. 1, pp. 67–87, 1999.

[18] K. Kärkkäinen, A. Sihvola, and K. Nikoskinen, "Effective permittivity of mixtures: Numerical validation by the FDTD mehod," *IEEE Trans. Geosci. Remote Sens.*, vol. 38, no. 3, pp. 1303–1308, 2000.

[19] K. Kärkkäinen, A. Sihvola, and K. Nikoskinen, "Analysis of a three-dimensional dielectric mixture with finite difference method," *IEEE Trans. Geosci. Remote Sens.*, vol. 39, no. 5, pp. 1013–1018, 2001.

[20] V. Myroshnychenko and C. Brosseau, "Finite-element method for calculation of the effective permittivity of random inhomogeneous media," *Physical Review E*, vol. 71, no. 1, pp. 016701:1–16, 2005.

[21] L. Jylhä and A. Sihvola, "Numerical modeling of disordered mixture using pseudorandom simulations," *IEEE Trans. Geosci. Remote Sens.*, vol. 43, no. 1, pp. 59–64, 2005.

[22] D. Wu, J. Chen, and C. Liu, "Numerical evaluation of effective dielectric properties of three-dimensional composite materials with arbitrary inclusions using a finite-difference time-domain method," *Journal of Applied Physics*, vol. 102, pp. 024107:1–8, 2007.

[23] T. Rylander, A. Bondeson, and P. Ingelström, *Computational Electromagnetics*. Springer, 2 ed., 2013.

[24] K. S. Yee, "Numerical solution of initial boundary value problems involving Maxwell's equations in isotropic media," *IEEE Trans. Antennas Propagat.*, vol. 14, no. 3, pp. 302–307, 1966.

[25] J. M. Jin, *The Finite Element Method in Electromagnetics*. John Wiley & Sons, 1993.

[26] E. Nyfors and P. Vainikainen, *Industrial Microwave Sensors*. Artech House, 1989.

[27] L. Cerullo, *Microwave Measurement Systems for In-line 3D Monitoring of Pharmaceutical Processes*. Ph.D. dissertation, Chalmers University of Technology, Göteborg, Sweden, 2013.

[28] A. Kraszewski, "Microwave aquametry - a review," *Journal of Microwave Power*, vol. 15, no. 4, pp. 209–220, 1980.

[29] S. O. Nelson, "Dielectric properties of agricultural products: measurements and applications," *IEEE Trans. Electr. Insul.*, vol. 26, no. 5, pp. 845–869, 1991.

[30] S. Trabelsi and S. O. Nelson, "Nondestructive sensing of physical properties of granular materials by microwave permittivity measurement," *IEEE Trans. Instrum. Meas.*, vol. 55, no. 3, pp. 953–963, 2006.

[31] N. E. Bengtsson and P. O. Risman, "Dielectric properties of foods at 3 GHz as determined by a cavity perturbation technique – part II: Measurements on food materials," *Journal of Microwave Power*, vol. 6, no. 2, pp. 107–123, 1971.

[32] C. Buschmüller, W. Wiedey, C. Döscher, J. Dressler, and J. Breitkreutz, "In-line monitoring of granule moisture in fluidized-bed dryers using microwave resonance technology," *European Journal of Pharmaceutics and Biopharmaceutics*, vol. 69, no. 1, pp. 380–387, 2008.

[33] V. Lourenço, T. Herdling, G. Reich, J. C. Menezes, and D. Lochmann, "Combining microwave resonance technology to multivariate data analysis as a novel PAT tool to improve process understanding in fluid bed granulation," *European Journal of Pharmaceutics and Biopharmaceutics*, vol. 78, no. 3, pp. 513–521, 2011.

[34] M. Tiuri, K. Jokela, and S. Heikkilä, "Microwave instrument for accurate moisture and density measurement of timber," *Journal of Microwave Power*, vol. 15, no. 4, pp. 251–254, 1980.

[35] M. Fischer, P. Vainikainen, and E. Nyfors, "Dual-mode stripline resonator array for fast error compensated moisture mapping of paper web," in *IEEE International Microwave Symposium Digest*, vol. 3, pp. 1133–1136, 1990.

[36] M. T. Hallikainen, F. T. Ulaby, M. C. Dobson, M. A. El-Rayes, and L.-K. Wu, "Microwave dielectric behavior of wet soil – Part I: Empirical models and experimental observations," *IEEE Trans. Geosci. Remote Sens.*, vol. 23, no. 1, pp. 25–34, 1985.

[37] A. Denoth, A. Foglar, P. Weiland, C. Mätzler, H. Aebischer, M. Tiuri, and A. Sihvola, "A comparative study of instruments for measuring the liquid water content of snow," *Journal of Applied Physics*, vol. 56, no. 7, pp. 2154–2160, 1984.

[38] M. Tiuri, A. Sihvola, E. Nyfors, and M. Hallikaiken, "The complex dielectric constant of snow at microwave frequencies," *IEEE Journal of Oceanic Engineering*, vol. 9, no. 5, pp. 377–382, 1984.

[39] A. Sihvola and M. Tiuri, "Snow fork for field determination of the density and wetness profiles of a snow pack," *IEEE Trans. Geosci. Remote Sens.*, vol. 24, no. 5, pp. 717–721, 1986.

[40] E. Nyfors, *Cylindrical Microwave Resonator Sensors for Measuring Materials Under Flow*. Ph.D. dissertation, Helsinki University of Technology, Helsinki, Finland, 2000.

[41] H. E. L. Ávila, D. J. Pagano, and F. R. Sousa, "Improving the performance of an RF resonant cavity water-cut meter using an impedance metching network," *Flow Measurement and Instrumentation*, vol. 43, pp. 14–22, 2015.

[42] K. Folgerø, T. Friisø, J. Hilland, and T. Tjomsland, "A broad-band and high-sensitivity dielectric spectroscopy measurement system for quality determination of low-permittivity fluids," *Meas. Sci. Technol.*, vol. 6, no. 7, pp. 995–1008, 1995.

[43] K. Folgerø, "Bilinear calibration of coaxial transmission/reflection cells for permittivity measurement of low-loss liquids," *Meas. Sci. Technol.*, vol. 7, no. 9, pp. 1260–1269, 1996.

[44] K. Folgerø, "Broad-band dielectric spectroscopy of low-permittivity fluids using one measurement cell," *IEEE Trans. Instrum. Meas.*, vol. 47, no. 4, pp. 881–885, 1998.

[45] Z. Wu, H. McKann, L. E. Davis, J. Hu, A. Fontes, and C. G. Xie, "Microwave-tomographic system for oil- and gas-multiphase-flow imaging," *Meas. Sci. Technol.*, vol. 20, no. 10, pp. 1–8, 2009.

[46] M. Mallach, P. Gebhardt, and T. Musch, "2D microwave tomography system for imaging of multiphase flows in metal pipes," *Flow Measurement and Instrumentation*, vol. 53, pp. 80–88, 2017.

[47] B. Jannier, O. Dubrunfaut, and F. Ossart, "Application of microwave reflectometry to disordered petroleum multiphase flow study," *Meas. Sci. Technol.*, vol. 24, no. 2, p. 025304, 2013.

[48] Y. Shirakawa, Y. Matsuo, J. Ohno, S. Watanabe, and H. Yashiro, "On-line measurement of particle size by microwave technology," *Nippon Steel Technical Report*, vol. 49, pp. 9–14, 1991.

[49] G. P. Hrin and D. T. Tuma, "Doppler microwave cavity monitor for particulate loading," *IEEE Trans. Instrum. Meas.*, vol. 26, no. 1, pp. 13–17, 1977.

[50] C. Baer, M. Vogt, and T. Musch, "Pseudo transmission measurement concept for the volume fraction determination of rice in a pneumatic conveying system," in *2012 International Conference on Electromagnetics in Advanced Applications (ICEAA)*, pp. 744–747, 2012.

[51] A. Penirschke and R. Jakoby, "Microwave mass flow detector for particulate solids based on spatial filtering velocimetry," *IEEE Trans. Microw. Theory Techn.*, vol. 56, no. 12, pp. 3193–3199, 2008.

[52] S. Kobayashi and S. Miyahara, "A particulate flow meter using microwaves," in *Proc. IMEKO*, (Prague), pp. 197–204, 1985.

[53] A. Penirschke, A. Angelovski, and R. Jakoby, "Helix-shaped CRLH-mass flow detector for the cross-sectional detection of inhomogeneous distributed pneumatic conveyed pulverized solids," in *Proc. 2011 IEEE Int. Instrum. Meas. Technol. Conf. (I2MTC), Binjiang, China*, pp. 1–5, 2011.

[54] G. Bailly, A. Harrabi, J. Rossignol, M. Michel, D. Stuerga, and P. Pribetich, "Microstrip spiral resonator for microwave-based gas sensing," *IEEE Sensors Letters*, vol. 1, no. 4, pp. 1–4, 2017.

[55] A. Merlo, "Combustion chamber investigations by means of microwave resonances," *IEEE Trans. Ind. Electron. Control Instrum.*, vol. 17, no. 2, pp. 60–66, 1970.

[56] G. Fischerauer, A. Gollwitzer, A. Nerowski, M. Spörl, and R. Moos, "On the inverse problem associated with the observation of electrochemical processes by the RF cavity perturbation method," in *2009 6th International Multi-Conference on Systems, Signals and Devices*, 2009.

[57] G. Fischerauer, M. Förster, and R. Moos, "Sensing the soot load in automotive diesel particulate filters by microwave methods," *Meas. Sci. Technol.*, vol. 21, no. 3, p. 035108, 2010.

[58] M. Abou-Khousa, A. Al-Durra, and K. Al-Wahedi, "Microwave sensing system for real-time monitoring of solid contaminants in gas flows," *IEEE Sensors J.*, vol. 15, no. 9, pp. 5296–5302, 2015.

[59] "Rosemount Tank Radar." Technical Description 501026En, 2012.

[60] M. Tiuri and H. Hyyryläinen, "Microwave radar for measuring vibrations on power transmission lines," in *1983 13th European Microwave Conference*, pp. 663–666, 1983.

[61] J. Hasch, E. Topak, R. Schnabel, T. Zwick, R. Weigel, and C. Waldschmidt, "Millimeter-wave technology for automotive radar sensors in the 77 GHz frequency band," *IEEE Trans. Microw. Theory Techn.*, vol. 60, no. 3, pp. 845–860, 2012.

[62] F. Engels, P. Heidenreich, A. M. Zoubir, F. K. Jondral, and M. Wintermantel, "Advances in automotive radar: A framework on computationally efficient high-resolution frequency estimation," *IEEE Signal Processing Magazine*, vol. 34, no. 2, pp. 36–46, 2017.

[63] V. A. Sydoruk, F. Fiorani, S. Jahnke, and H.-J. Krause, "Design and characterization of microwave cavity resonators for noninvasive monitoring of plant water distribution," *IEEE Trans. Microw. Theory Techn.*, vol. 64, no. 9, pp. 2894–2904, 2016.

[64] D. J. Rowe, S. al-Malki, A. A. Abduljabar, A. Porch, D. A. Barrow, and C. J. Allender, "Improved split-ring resonator for microfluidic sensing," *IEEE Trans. Microw. Theory Techn.*, vol. 62, no. 3, pp. 689–699, 2014.

[65] A. A. Abduljabar, D. J. Rowe, A. Porch, and D. A. Barrow, "Novel microwave microfluidic sensor using a microstrip split-ring resonator," *IEEE Trans. Microw. Theory Techn.*, vol. 62, no. 3, pp. 679–688, 2014.

[66] M. Persson, A. Fhager, H. Dobšíček Trefná, Y. Yu, T. McKelvey, G. Pegenius, J. E. Karlsson, and M. Elam, "Microwave-based stroke diagnosis making global prehospital thrombolytic treatment possible," *IEEE Trans. Biomed. Eng.*, vol. 61, no. 11, pp. 2806–2817, 2014.

[67] E. C. Fear, X. Li, S. C. Hagness, and M. A. Stuchly, "Confocal microwave imaging for breast cancer detection: Localization of tumors in three dimensions," *IEEE Trans. Biomed. Eng.*, vol. 49, no. 8, pp. 812–822, 2002.

[68] B. W. Hakki and P. D. Coleman, "A dielectric resonator method of measuring inductive capacities in the millimeter range," *IRE Transactions on Microwave Theory and Techniques*, vol. 8, no. 4, pp. 402–410, 1960.

[69] J. Krupka, "Frequency domain complex permittivity measurements at microwave frequencies," *Meas. Sci. Technol.*, vol. 17, no. 6, pp. 55–70, 2006.

[70] M. D. Janezic, E. F. Kuester, and J. Baker-Jarvis, "Broadband complex permittivity measurements of dielectric substrates using a split-cylinder resonator," in *2004 IEEE MTT-S International Microwave Symposium Digest*, pp. 1817–1820, 2004.

[71] D. J. Rowe, A. Porch, D. A. Barrow, and C. J. Allender, "Novel coupling structure for the resonant coaxial probe," *IEEE Trans. Microw. Theory Techn.*, vol. 60, no. 6, pp. 1699–1708, 2012.

[72] D. J. Rowe, A. Porch, D. A. Barrow, and C. J. Allender, "Microfluidic microwave sensor for simultaneous dielectric and magnetic characterization," *IEEE Trans. Microw. Theory Techn.*, vol. 61, no. 1, pp. 234–243, 2013.

[73] A. Angelovski, A. Penirschke, and R. Jakoby, "CRLH-mass flow detector array for cross-sectional detection of inhomogeneous distributed flow regimes in pipelines," in *2011 41st European Microwave Conference (EuMC), Manchester, UK*, pp. 611–614, 2011.

[74] J. Nohlert, L. Cerullo, J. Winges, T. Rylander, T. McKelvey, A. Holmgren, L. Gradinarsky, S. Folestad, M. Viberg, and A. Rasmuson, "Global monitoring of fluidized-bed processes by means of microwave cavity resonances," *Measurement*, vol. 55, pp. 520–535, 2014.

[75] D. Pozar, *Microwave Engineering*. John Wiley & Sons, 2 ed., 1998.

[76] C. A. Balanis, *Advanced Engineering Electromagnetics*. John Wiley & Sons, 1989.

[77] E. L. Ginzton, *Microwave Measurements*. McGraw-Hill, 1957.

[78] R. L. Sproull and E. G. Linder, "Resonant-cavity measurements," *Proceedings of the IRE*, vol. 34, no. 5, pp. 305–312, 1946.

[79] G. Birnbaum and J. Franeau, "Measurement of the dielectric constant and loss of solids and liquids by a cavity perturbation method," *Journal of Applied Physics*, vol. 20, no. 8, pp. 817–818, 1949.

[80] H. A. Bethe and J. Schwinger, "Perturbation theory for cavities." M.I.T. Radiation Laboratory Report DI-117, March 1943.

[81] J. C. Slater, "Microwave electronics," *Rev. Mod. Phys.*, vol. 18, no. 4, pp. 441–512, 1946.

[82] R. F. Harrington, *Time-Harmonic Electromagnetic Fields*. McGraw-Hill, 1961.

[83] J. A. Stratton, *Electromagnetic Theory*. McGraw-Hill, 1941. Chapter III, p. 211.

[84] A. Parkash, J. K. Vaid, and A. Mansingh, "Measurement of dielectric parameters at microwave frequencies by cavity-perturbation technique," *IEEE Trans. Microw. Theory Techn.*, vol. 27, no. 9, pp. 791–795, 1979.

[85] B. Meng, J. Booske, and R. Cooper, "Extended cavity perturbation technique to determine the complex permittivity of dielectric materials," *IEEE Trans. Microw. Theory Techn.*, vol. 43, no. 11, pp. 2633–2636, 1995.

[86] K. B. Yu, S. G. Ogourtsov, V. G. Belenky, A. B. Maslenikov, and A. S. Omar, "Accurate microwave resonant method for complex permittivity measurements of liquids," *IEEE Trans. Microw. Theory Techn.*, vol. 48, no. 11, pp. 2159–2164, 2000.

[87] M. Lin and M. N. Afsar, "A new cavity perturbation technique for accurate measurement of dielectric parameters," in *2006 IEEE MTT-S International Microwave Symposium Digest*, pp. 1630–1633, 2006.

[88] R. G. Carter, "Accuracy of microwave cavity perturbation measurements," *IEEE Trans. Microw. Theory Techn.*, vol. 49, no. 5, pp. 918–923, 2001.

[89] R. Coccioli, G. Pelosi, and S. Selleri, "Characterization of dielectric materials with the finite-element method," *IEEE Trans. Microw. Theory Techn.*, vol. 47, no. 7, pp. 1106–1112, 1999.

[90] S. Günel and E. Y. Zoral, "Parametric history analysis for material properties using finite elements and adaptive perturbations," *IEEE Trans. Microw. Theory Techn.*, vol. 63, no. 1, pp. 90–98, 2015.

[91] T. P. Wangler, *RF Linear Accelerators*. John Wiley & Sons, 2 ed., 2008.

[92] D. A. Engers, M. N. Fricke, R. P. Storey, A. W. Newman, and K. R. Morris, "Triboelectrification of pharmaceutically relevant powders during low-shear tumble blending," *J. Electrostat.*, vol. 64, pp. 826–835, 2006.

[93] P. J. Petersan and S. M. Anlage, "Measurement of resonant frequency and quality factor of microwave resonators: Comparison of methods," *Journal of Applied Physics*, vol. 84, no. 6, pp. 3392–3402, 1998.

[94] D. Kajfez, "Graphical analysis of Q circuits," *IEEE Trans. Microw. Theory Techn.*, vol. 11, no. 5, pp. 453–454, 1963.

[95] K. Leong and J. Mazierska, "Precise measurements of the Q factor of dielectric resonators in the transmission mode – accounting for noise, crosstalk, delay of uncalibrated lines, coupling loss, and coupling reactance," *IEEE Trans. Microw. Theory Techn.*, vol. 50, no. 9, pp. 2115–2127, 2002.

[96] D. Kajfez, "Linear fractional curve fitting for measurement of high Q factors," *IEEE Trans. Microw. Theory Techn.*, vol. 42, no. 7, pp. 1149–1153, 1994.

[97] R. Pintelon, P. Guillaume, Y. Rolain, J. Schoukens, and H. Van Hamme, "Parametric identification of transfer functions in the frequency domain – a survey," *IEEE Trans. Autom. Control*, vol. 39, no. 11, pp. 2245–2260, 1994.

[98] T. McKelvey, H. Akçay, and L. Ljung, "Subspace-based multivariable system identification from frequency response data," *IEEE Trans. Autom. Control*, vol. 41, no. 7, pp. 960–979, 1996.

[99] "Keysight Microwave Transceiver N7081A, Data Sheet and Technical Overview." Keysight Technologies, N7081-90002, 2015.

[100] H. E. L. Ávila, F. R. Sousa, and D. J. Pagano, "Resonant cavity water cut meter with automatic resonance tracking system," in *2017 IEEE International Instrumentation and Measurement Technology Conference (I2MTC)*, pp. 1–6, 2017.

[101] J. Markowski, A. D. MacDonald, and S. S. Stuchly, "The dynamic response of a resonant frequency tracking system," *IEEE Trans. Instrum. Meas*, vol. 26, no. 3, pp. 231–237, 1977.

[102] X. Zheng, A. Fhager, M. Persson, P. Linner, and H. Zirath, "Accuracy evaluation of ultrawideband time domain systems for microwave imaging," *IEEE Trans. Antennas Propagat.*, vol. 59, no. 11, pp. 4279–4285, 2011.

[103] M. A. Abou-Khousa, M. A. Baumgartner, S. Kharkovsky, and R. Zoughi, "Novel and simple high-frequency single-port vector network analyzer," *IEEE Trans. Instrum. Meas.*, vol. 59, no. 3, pp. 534–542, 2010.

[104] S. Corbellini, "A low-cost instrument for the measurement of microwave resonances in quasi-spherical cavities," in *2012 IEEE International Instrumentation and Measurement Technology Conference (I2MTC)*, pp. 641–646, 2012.

[105] J. Nehring, M. Dietz, K. Aufinger, G. Fischer, R. Weigel, and D. Kissinger, "A 4–32-GHz chipset for a highly integrated heterodyne two-port vector network analyzer," *IEEE Trans. Microw. Theory Techn.*, vol. 64, no. 3, pp. 892–905, 2016.

[106] J. Nehring, M. Schütz, M. Dietz, I. Nasr, K. Aufinger, R. Weigel, and D. Kissinger, "Highly integrated 4–32-GHz two-port vector network analyzers for instrumentation and biomedical applications," *IEEE Trans. Microw. Theory Techn.*, vol. 65, no. 1, pp. 229–244, 2017.

[107] S. M. Kay, *Fundamentals of Statistical Signal Processing: Estimation Theory*. Prentice Hall, 1993.

[108] T. Fawcett, "An introduction to ROC analysis," *Pattern Recognition Letters*, vol. 27, no. 8, pp. 861–874, 2006.

[109] S. M. Kay, *Fundamentals of Statistical Signal Processing: Detection Theory*. Prentice Hall, 1998.

[110] T. Hastie, R. Tibshirani, and J. Friedman, *The Elements of Statistical Learning: Data Mining, Inference, and Prediction*. Springer, 2 ed., 2009.

[111] G. Grimmett and D. Stirzaker, *Probability and Random Processes*. Oxford University Press, 2001.

[112] J. G. Proakis and D. G. Manolakis, *Digital Signal Processing: Principles, Algorithms and Applications*. Prentice Hall, 4 ed., 2007.

[113] P. Stoica and R. Moses, *Spectral Analysis of Signals*. Prentice Hall, 2005.

[114] R. G. Gallager, *Principles of Digital Communication*. Cambridge University Press, 2008.

[115] E. K. Miller, "Model-based parameter estimation in electromagnetics. Part I. Background and theoretical development," *IEEE Antennas and Propagation Magazine*, vol. 40, no. 1, pp. 42–52, 1998.

[116] S. D. Fisher, *Complex Variables*. Dover Publications, 2 ed., 1999.

[117] K. Fischer, "Neues verfahren zur maßanalytischen bestimmung des wassergehaltes von flüssigkeiten und festen körpern," *Angewandte Chemie*, vol. 48, no. 26, pp. 394–396, 1935.

[118] T. De Beer, A. Burggraeve, M. Fonteyne, L. Saerens, J. P. Remon, and C. Vervaet, "Near infrared and Raman spectroscopy for the in-process monitoring of pharmaceutical production processes," *International Journal of Pharmaceutics*, vol. 417, pp. 32–47, 2011.

[119] V. Rimpiläinen, L. M. Heikkinen, and M. Vauhkonen, "Moisture distribution and hydrodynamics of wet granules during fluidized-bed drying characterized with volumetric electrical capacitance tomography," *Chemical Engineering Science*, vol. 75, pp. 220–234, 2012.

[120] "Comsol Multiphysics." http://www.comsol.com, 2018.

[121] M. Graves, A. Smith, and B. Batchelor, "Approaches to foreign body detection in foods," *Trends in Food Science & Technology*, vol. 9, no. 1, pp. 21–27, 1998.

[122] D. Sun, Y. Yan, R. M. Carter, L. Gao, G. Lu, G. Riley, and M. Wood, "On-line nonintrusive detection of wood pellets in pneumatic conveying pipelines using vibration and acoustic sensors," *IEEE Trans. Instrum. Meas.*, vol. 63, no. 5, pp. 993–1001, 2014.

[123] B. K. Cho and J. M. K. Irudayaraj, "Foreign object and internal disorder detection in food materials using noncontact ultrasound imaging," *Journal of Food Science*, vol. 68, no. 3, pp. 967–974, 2003.

[124] E. Hæggström and M. Luukkala, "Ultrasound detection and identification of foreign bodies in food products," *Food Control*, vol. 12, no. 1, pp. 37–45, 2001.

[125] G. Ginesu, D. D. Giusto, V. Märgner, and P. Meinlschmidt, "Detection of foreign bodies in food by thermal image processing," *IEEE Trans. Ind. Electron.*, vol. 51, no. 2, pp. 480–490, 2004.

[126] Y.-K. Lee, S.-W. Choi, S.-T. Han, D. H. Woo, and H. S. Chun, "Detection of foreign bodies in foods using continuous wave terahertz imaging," *Journal of Food Protection*, vol. 75, no. 1, pp. 179–183, 2012.

[127] "Metal detection solutions: Powder and granular product applications." Mettler-Toledo, http://www.mt.com/metaldetection, 2018.

Appended papers